



# The Lyman Continuum Escape Fraction of Star-forming Galaxies at $2.4 \lesssim z \lesssim 3.0$ from UVCANDELS

Xin Wang<sup>1,2,3</sup> , Harry I. Teplitz<sup>4</sup> , Brent M. Smith<sup>5</sup> , Rogier A. Windhorst<sup>5</sup> , Marc Rafelski<sup>6,7</sup> , Vihang Mehta<sup>4</sup> , Anahita Alavi<sup>4</sup> , Zhiyuan Ji<sup>8</sup> , Gabriel Brammer<sup>9,10</sup> , James Colbert<sup>4</sup> , Norman Grogin<sup>6</sup> , Nimish P. Hathi<sup>6</sup> , Anton M. Koekemoer<sup>6</sup> , Laura Prichard<sup>6</sup> , Claudia Scarlata<sup>11</sup> , Ben Sunnquist<sup>6</sup> , Pablo Arrabal Haro<sup>12</sup> , Christopher Conselice<sup>13</sup> , Eric Gawiser<sup>14</sup> , Yicheng Guo<sup>15</sup> , Matthew Hayes<sup>16</sup> , Rolf A. Jansen<sup>5</sup> , Ray A. Lucas<sup>6</sup> , Robert O’Connell<sup>17</sup> , Brant Robertson<sup>18</sup> , Michael Rutkowski<sup>19</sup> , Brian Siana<sup>20</sup> , Eros Vanzella<sup>21</sup> , Teresa Ashcraft<sup>5</sup> , Micaela Bagley<sup>22</sup> , Ivano Baronchelli<sup>23,24</sup> , Guillermo Barro<sup>25</sup> , Alex Blanche<sup>5</sup> , Adam Broussard<sup>14</sup> , Timothy Carleton<sup>5</sup> , Nima Chartab<sup>26</sup> , Yingjie Cheng<sup>27</sup> , Alex Codoreanu<sup>28</sup> , Seth Cohen<sup>5</sup> , Y. Sophia Dai<sup>2</sup> , Behnam Darvish<sup>20</sup> , Romeel Dave<sup>29</sup> , Laura DeGroot<sup>30</sup> , Duilia De Mello<sup>31</sup> , Mark Dickinson<sup>12</sup> , Najmeh Emami<sup>20</sup> , Henry Ferguson<sup>6</sup> , Leonardo Ferreira<sup>32</sup> , Keely Finkelstein<sup>22</sup> , Steven Finkelstein<sup>22</sup> , Jonathan P. Gardner<sup>33</sup> , Timothy Gburek<sup>20</sup> , Mauro Giavalisco<sup>8</sup> , Andrea Grazian<sup>23</sup> , Caryl Gronwall<sup>34,35</sup> , Shoubaneh Hemmati<sup>4</sup> , Justin Howell<sup>4</sup> , Kartheik Iyer<sup>36</sup> , Sugata Kaviraj<sup>37</sup> , Peter Kurczynski<sup>33</sup> , Ilin Lazar<sup>38</sup> , John MacKenty<sup>6</sup> , Kameswara Bharadwaj Mantha<sup>11</sup> , Alec Martin<sup>15</sup> , Garreth Martin<sup>39,40</sup> , Tyler McCabe<sup>5</sup> , Bahram Mobasher<sup>20</sup> , Kalina Nedkova<sup>7</sup> , Charlotte Olsen<sup>14</sup> , Lillian Otteson<sup>5</sup> , Swara Ravindranath<sup>6</sup> , Caleb Redshaw<sup>5</sup> , Zahra Sattari<sup>20</sup> , Emmaris Soto<sup>41</sup> , L. Y. Aaron Yung<sup>33</sup> , Bonnabelle Zabelle<sup>11</sup> , and the UVCANDELS team

- <sup>1</sup> School of Astronomy and Space Science, University of Chinese Academy of Sciences (UCAS), Beijing 100049, People’s Republic of China; [xwang@ucas.ac.cn](mailto:xwang@ucas.ac.cn)
- <sup>2</sup> National Astronomical Observatories, Chinese Academy of Sciences, Beijing 100101, People’s Republic of China
- <sup>3</sup> Institute for Frontiers in Astronomy and Astrophysics, Beijing Normal University, Beijing 102206, People’s Republic of China
- <sup>4</sup> IPAC, Mail Code 314-6, California Institute of Technology, 1200 E. California Blvd., Pasadena CA 91125, USA
- <sup>5</sup> School of Earth and Space Exploration, Arizona State University, Tempe, AZ 85287, USA
- <sup>6</sup> Space Telescope Science Institute, Baltimore, MD 21218, USA
- <sup>7</sup> Department of Physics and Astronomy, Johns Hopkins University, Baltimore, MD 21218, USA
- <sup>8</sup> Department of Astronomy, University of Massachusetts, Amherst, MA 01003, USA
- <sup>9</sup> Cosmic Dawn Center (DAWN), Denmark
- <sup>10</sup> Niels Bohr Institute, University of Copenhagen, Jagtvej 128, DK-2200 Copenhagen N, Denmark
- <sup>11</sup> Minnesota Institute of Astrophysics and School of Physics and Astronomy, University of Minnesota, Minneapolis, MN 55455, USA
- <sup>12</sup> NSF’s NOIRLab, Tucson, AZ 85719, USA
- <sup>13</sup> School of Physics and Astronomy, The University of Nottingham, University Park, Nottingham, NG7 2RD, UK
- <sup>14</sup> Department of Physics and Astronomy, Rutgers, The State University of New Jersey, Piscataway, NJ 08854, USA
- <sup>15</sup> Department of Physics and Astronomy, University of Missouri, Columbia, MO 65211, USA
- <sup>16</sup> Department of Astronomy and Oskar Klein Centre for Cosmoparticle Physics, Stockholm University, AlbaNova University Centre, SE-10691, Stockholm, Sweden
- <sup>17</sup> Department of Astronomy, University of Virginia, Charlottesville, VA 22904, USA
- <sup>18</sup> Department of Astronomy and Astrophysics, University of California, Santa Cruz, Santa Cruz, CA 95064, USA
- <sup>19</sup> Department of Physics and Astronomy, Minnesota State University Mankato, Mankato, MN 56001, USA
- <sup>20</sup> Department of Physics and Astronomy, University of California, Riverside, Riverside, CA 92521, USA
- <sup>21</sup> INAF—OAS, Osservatorio di Astrofisica e Scienza dello Spazio di Bologna, via Gobetti 93/3, I-40129 Bologna, Italy
- <sup>22</sup> Department of Astronomy, The University of Texas at Austin, Austin, TX 78712, USA
- <sup>23</sup> INAF—Osservatorio Astronomico di Padova, Vicolo dell’Osservatorio 5, I-35122 Padova, Italy
- <sup>24</sup> Dipartimento di Fisica e Astronomia, Università di Padova, vicolo Osservatorio, 3, I-35122 Padova, Italy
- <sup>25</sup> Department of Physics, University of the Pacific, Stockton, CA 95211, USA
- <sup>26</sup> Observatories of the Carnegie Institution of Washington, Pasadena, CA 91101, USA
- <sup>27</sup> Department of Astronomy, University of Massachusetts, Amherst, 01003 MA, USA
- <sup>28</sup> Centre for Astrophysics and Supercomputing, Swinburne University of Technology, Hawthorn, VIC 3122, Australia
- <sup>29</sup> Institute for Astronomy, University of Edinburgh, Edinburgh, EH9 3HJ, UK
- <sup>30</sup> College of Wooster, Wooster, OH 44691, USA
- <sup>31</sup> Department of Physics, The Catholic University of America, Washington, DC 20064, USA
- <sup>32</sup> Centre for Astronomy and Particle Physics, School of Physics and Astronomy, University of Nottingham, Nottingham, NG7 2RD, UK
- <sup>33</sup> Astrophysics Science Division, NASA Goddard Space Flight Center, Greenbelt, MD 20771, USA
- <sup>34</sup> Department of Astronomy & Astrophysics, The Pennsylvania State University, University Park, PA 16802, USA
- <sup>35</sup> Institute for Gravitation and the Cosmos, The Pennsylvania State University, University Park, PA 16802, USA
- <sup>36</sup> Dunlap Institute for Astronomy & Astrophysics, University of Toronto, 50 St George Street, Toronto, ON M5S 3H4, CA
- <sup>37</sup> Centre for Astrophysics Research, Department of Physics, Astronomy and Mathematics, University of Hertfordshire, Hatfield, AL10 9AB, UK
- <sup>38</sup> Department of Galaxies and Cosmology, Max Planck Institute for Astronomy, Königstuhl 17, 69117 Heidelberg, Germany
- <sup>39</sup> Korea Astronomy and Space Science Institute, Yuseong-gu, Daejeon 34055, Republic of Korea
- <sup>40</sup> Steward Observatory, University of Arizona, Tucson, AZ 85719, USA
- <sup>41</sup> Computational Physics, Inc., Springfield, VA 22151, USA

Received 2023 January 1; revised 2024 December 19; accepted 2024 December 30; published 2025 February 5



Original content from this work may be used under the terms of the [Creative Commons Attribution 4.0 licence](https://creativecommons.org/licenses/by/4.0/). Any further distribution of this work must maintain attribution to the author(s) and the title of the work, journal citation and DOI.

## Abstract

The UltraViolet Imaging of the Cosmic Assembly Near-infrared Deep Extragalactic Legacy Survey Fields (UVCANDELS) survey is a Hubble Space Telescope (HST) Cycle-26 Treasury Program, allocated in total 164 orbits of primary Wide-Field Camera 3 Ultraviolet and VISible light F275W imaging with coordinated parallel Advanced Camera for Surveys F435W imaging, on four of the five premier extragalactic survey fields: GOODS-N, GOODS-S, EGS, and COSMOS. We introduce this survey by presenting a comprehensive analysis of the absolute escape fraction ( $f_{\text{esc}}^{\text{abs}}$ ) of Lyman continuum radiation through stacking the UV images of a population of star-forming galaxies with secure redshifts at  $2.4 \leq z \leq 3.0$ . Our stacking benefits from the catalogs of high-quality spectroscopic redshifts compiled from archival ground-based data and HST slitless spectroscopy, carefully vetted by dedicated visual inspection efforts. We develop a robust stacking method to apply to 10 samples of in total 56 galaxies, and perform detailed Monte Carlo simulations of the intergalactic medium (IGM) attenuation, to take into account the sample variance of the mean IGM transmission when measuring  $f_{\text{esc}}^{\text{abs}}$ . The full stack at  $z \approx 2.44$  from 28 galaxies places a stringent  $1\sigma$  upper limit of  $f_{\text{esc}}^{\text{abs}} \lesssim 5\%$ , whereas the full stack at  $z \approx 2.72$  of an equal number of galaxies gives an upper limit of  $f_{\text{esc}}^{\text{abs}} \lesssim 26\%$  at  $1\sigma$  confidence level. These new F275W and F435W imaging mosaics from UVCANDELS have been made publicly available on the Barbara A. Mikulski Archive for Space Telescopes.

*Unified Astronomy Thesaurus concepts:* [Reionization \(1383\)](#); [Intergalactic medium \(813\)](#); [Ultraviolet surveys \(1742\)](#); [High-redshift galaxies \(734\)](#); [Galaxy evolution \(594\)](#)

## 1. Introduction

Cosmic reionization is the last major phase transition of the Universe when its bulk properties are altered by galaxies (see, e.g., X. Fan et al. 2006; D. P. Stark 2016). There has been increasing evidence that young massive stars collectively dominate over supermassive black holes in the early Universe in producing the Lyman continuum (LyC) photons (with rest-frame wavelength  $\lambda_{\text{rest}} < 912 \text{ \AA}$ ) that reionize the neutral intergalactic medium (IGM) at  $z \sim 6\text{--}9$  (P. Dayal et al. 2020). However, the exact fraction of these LyC photons that evade photoelectric and dust absorption from their origin galaxy and escape into the IGM to ionize it,  $f_{\text{esc}}$ , remains elusive and controversial (S. L. Finkelstein et al. 2019; R. P. Naidu et al. 2020), making  $f_{\text{esc}}$  one of the greatest unknowns in reionization studies. Furthermore, the intervening IGM transmission drops precipitously at  $z \geq 4$ , due to the steeply rising IGM opacity,  $\tau_{\text{IGM}}$  (A. K. Inoue et al. 2014). As a result, it is basically impractical to directly measure any LyC leakage in the Epoch of Reionization (EoR).

A more feasible way forward is thus to find low-redshift galaxies that are analogous to those  $\gtrsim 13$  Gyr ago, which are thought to drive the reionization process. The constraints and measurements of their LyC  $f_{\text{esc}}$  and its correlation with their physical properties can help shed light upon the detailed physical mechanism conducive to the escape of the ionizing radiation into the IGM, surviving the absorption by the intervening H I gas and dust in the interstellar medium (ISM) or circumgalactic medium (C. C. Steidel et al. 2018).

Due to the intrinsic faintness of LyC flux, the searches for LyC leakage at any cosmological distances have been very challenging. Generally speaking, currently available ultraviolet (UV) instrumentation leads to fruitful detection of LyC leakage at primarily two redshift windows. One is at  $z \sim 0.3$ , where LyC can be captured by the space-based far-UV spectroscopy (see, e.g., C. Leitherer et al. 1995; N. Bergvall et al. 2006; S. Borthakur et al. 2014; Y. I. Izotov et al. 2016, 2018). The recent Hubble Space Telescope (HST) Cosmic Origin Spectrograph campaigns have led to the detection of LyC signals in several dozen targets at  $z \sim 0.3$ , which are usually compact isolated galaxies with high ionization and extreme star formation, a.k.a. Green Peas (GPs; see, e.g., Y. I. Izotov et al. 2021; S. R. Flury et al. 2022). Yet the complex selection

function and dissimilar environments of these  $z \sim 0.3$  GPs make it difficult to generalize these findings to the EoR (R. P. Naidu et al. 2021).

The other major redshift range, much closer to the EoR in time, is at  $z \sim 2\text{--}3$  where LyC flux is accessible to ground-based blue-sensitive instruments (see, e.g., F. Marchi et al. 2018; C. C. Steidel et al. 2018; A. J. Pahl et al. 2021; A. Saxena et al. 2022) or HST Wide-Field Camera 3 (WFC3) Ultraviolet and VISible light (UVIS) imaging (see, e.g., E. Vanzella et al. 2016; F.-Y. Bian et al. 2017; R. P. Naidu et al. 2017; T. J. Fletcher et al. 2019; T. E. Rivera-Thorsen et al. 2019; F.-T. Yuan et al. 2021; L. J. Prichard et al. 2022). These studies are progressively reaching a consensus in support of an intriguing bimodality of  $f_{\text{esc}}$ . On one hand, there exists a population of sources with super- $L_*$  UV luminosities that leak a surprisingly large amount of ionizing radiation with  $f_{\text{esc}} \gtrsim 50\%$ , e.g., ION1 at  $z = 3.8$  (E. Vanzella et al. 2012; Z. Ji et al. 2020), ION2 at  $z = 3.2$  (S. d. Barros et al. 2016; E. Vanzella et al. 2016), ION3 at  $z = 4$  (E. Vanzella et al. 2018), the SUNBURST arc at  $z = 2.37$  (T. E. Rivera-Thorsen et al. 2019), Q1549-C25 at  $z = 3.2$  (A. E. Shapley et al. 2016), etc. On the other hand, there are far more galaxies on which only upper limits can be derived, despite deep imaging and spectroscopy (tens of hours of integration on a 8/10 m diameter ground-based telescope or HST; M. A. Malkan et al. 2003; B. D. Siana et al. 2007, 2010; B. Siana et al. 2015; K. Vasei et al. 2016; A. Alavi et al. 2020). Stacking these nondetections produces population-averaged  $f_{\text{esc}}$  with tight upper limits of 5%–10% for  $\gtrsim 0.5L_*$  galaxies at  $z \sim 3$  (M. J. Rutkowski et al. 2017; C. C. Steidel et al. 2018; R. Begley et al. 2022). At face value, this tight upper limit does not bode well for the completion of reionization by  $z \sim 6$ , which requires  $f_{\text{esc}} \sim 10\%\text{--}20\%$  under the canonical reionization picture (B. E. Robertson et al. 2013, 2015). This crisis can be largely alleviated, though, if one or several of the following conditions are met. (1) Galaxies produce and leak ionizing photons more efficiently at higher redshifts and lower stellar mass (S. L. Finkelstein et al. 2019; S. Mascia et al. 2023; H. Atek et al. 2024). (2) Reionization is instead driven by a much rarer class of massive, bright galaxies ( $M_{\text{UV}} \lesssim -20$  and  $M_* \gtrsim 10^{8.5} M_{\odot}$ ) with much higher  $f_{\text{esc}}$  and ionizing photon production efficiency (the oligarch scenario; R. P. Naidu et al.

2020, 2021). (3) The completion of reionization is delayed to a redshift of  $z \sim 5$  (G. Kulkarni et al. 2019). Furthermore,  $f_{\text{esc}}$  is closely tied to other galaxy properties (stellar mass, star formation rate, hereafter SFR, stellar initial mass function, metallicity, etc.), while the overall emissivity caused by the entire galaxy population also depends on the shape and cutoff of the luminosity function.

The Ultraviolet Imaging of the Cosmic Assembly Near-infrared Deep Extragalactic Legacy Survey Fields (UVCANDELS) survey is an HST Cycle-26 Treasury Program (HST-GO-15647, PI: Teplitz), awarded a sum of 164 orbits of primary Wide Field Camera 3 (WFC3) UVIS/F275W imaging with coordinated parallel Advanced Camera for Survey (ACS) F435W imaging, on four of the five premier extragalactic survey fields: GOODS-N, GOODS-S, EGS, and COSMOS. The UVCANDELS data set is unique in further testing the LyC leakage bimodality mentioned above, since it is the uniform UV data set surveying the largest area with UVIS, amounting to  $\sim 426 \text{ arcmin}^2$ , with extensive spectroscopic redshift measurements. The UV images across the entire fields, reaching a  $5\sigma$  sensitivity of  $\text{mag}_{\text{F275W}} = 27$  for compact sources, are taken at Hubble’s angular resolution. This is critical, since a key necessity in LyC searches is to confirm the origin of these faint signals with high-spatial-resolution imaging/spectroscopy, in order to exclude the possibility of foreground contamination from low- $z$  interlopers along the line of sight (see, e.g., C. C. Steidel et al. 2001; I. Iwata et al. 2009; E. Vanzella et al. 2010, 2012; D. B. Nestor et al. 2011, 2013; R. E. Mostardi et al. 2013).

This paper is organized as follows. In Section 2, we first present a comprehensive overview of the key science drivers of the UVCANDELS Treasury Program. In Section 3, we present the observing strategy and data reduction details. We then explain the selection of our galaxy sample with spectroscopic redshifts in Section 4. In Section 5, we describe our image stacking techniques and show the results. The inference of the LyC  $f_{\text{esc}}$  is given in Section 6. Finally, we conclude in Section 7. Throughout this paper, the standard AB magnitude system is used (J. B. Oke & J. E. Gunn 1983).

## 2. Science Overview of UVCANDELS

UVCANDELS provides extensive UVIS imaging in four of the five premier HST deep-wide survey fields: GOODS-N, GOODS-S, EGS, and COSMOS, targeted by the Cosmic Assembly Near-infrared Deep Extragalactic Legacy Survey (CANDELS; N. A. Grogin et al. 2011; A. M. Koekemoer et al. 2011). UVCANDELS takes primary WFC3 F275W exposures at a uniform three orbit depth and coordinated parallel ACS F435W exposures at a slightly varying depth resulting from the roll angle constraints and the overlap from the increased field of view (FoV) of the ACS camera. In total, the UV coverage secured by UVCANDELS reaches  $\sim 426 \text{ arcmin}^2$ , a factor of 2.7 larger than all previous data combined, including the WFC3 Early Release Science (ERS) UVIS imaging in GOODS-South (R. A. Windhorst et al. 2011), the CANDELS F275W Continuous Viewing Zone (CVZ) imaging in GOODS-North (N. A. Grogin et al. 2011), the UVUDF imaging in the Hubble Ultradeep Field within GOODS-South (H. I. Teplitz et al. 2013; M. A. Rafelski et al. 2015), and the HDUV covering portions of both GOODS fields (P. A. Oesch et al. 2018).<sup>42</sup>

<sup>42</sup> The number of pointings in each UVCANDELS fields are 16 in GOODS-N, 8 in GOODS-S, 20 in EGS, and 16 in COSMOS.

This unique data set enables a wide range of scientific explorations as follows (X. Wang et al. 2020):

1. Using the high-spatial-resolution UV and blue data (700 pc at  $z \sim 1$ ) to study the structural evolution of galaxies and create 2D maps of their star formation history (SFH).
2. Combining UVCANDELS with the valuable Herschel legacy far-infrared data to trace the evolution of the star formation, gas, and dust content of moderate redshift ( $z < 1$ ) galaxies.
3. Probing the role of environment in the evolution of low-mass ( $\lesssim 10^9 M_{\odot}$ ) star-forming galaxies at  $z \sim 1$ .
4. Investigating the decay of star formation in massive early type galaxies and the role of minor mergers since  $z \sim 1.5$ .
5. Constraining the escape fraction of ionizing radiation (with  $\lambda_{\text{rest}} \leq 912 \text{ \AA}$ ) from galaxies at  $z \gtrsim 2.4$  to better understand how star-forming galaxies reionized the Universe at  $z > 6$ .

In addition, this unique UVCANDELS data set has additional treasury value: UV data break the degeneracy between the Balmer break and Lyman break spectral features (M. A. Rafelski et al. 2015) to improve the photo- $z$  accuracy. HST UV data complement the existing and newly obtained ground-based U-band surveys in the CANDELS fields (T. A. Ashcraft et al. 2018; C. Redshaw et al. 2022).

## 3. Observations and Data Reduction

### 3.1. UVCANDELS Observations

The UVCANDELS program (HST-GO-15647, PI: Teplitz) obtained F275W and F435W (coordinated parallel) imaging of four of the CANDELS fields (see Figure 1), providing new UV (F275W) and wide-area blue optical (F435W) coverage in the COSMOS and EGS fields, and doubling the UV area in GOODS.

The survey was designed to reach a  $5\sigma$  limiting magnitude of  $\text{mag}_{\text{F275W}} = 27$  for compact galaxies (with  $0''.2$  radius), which corresponds to an unobscured SFR limit of  $0.2 M_{\odot} \text{ yr}^{-1}$  at  $z \sim 1$ . This goal required about 8100 s per pointing in F275W (three orbits of two  $\sim 1350$  s exposures each). A minimum of six exposures were required for good rejection of cosmic rays (CR), which was determined using the archival UVUDF H. I. Teplitz et al. (2013) data set. As a result, UVCANDELS did not choose the full-orbit exposures that are optimized for deep surveys with greater on-sky redundancy. In GOODS-N, CVZ increased the efficiency of the observations.

Following the Space Telescope Science Institute’s best practices, exposures included postflash to mitigate the effects of UVIS charge transfer efficiency (CTE) degradation (J. W. Mackenty & L. Smith 2012). Postflash protects against the loss of the faintest objects by filling “traps” on the charge-coupled devices (CCDs) before readout. The selected postflash level brings the on-chip background up to  $12 e^-$  per pixel on average.

The F435W parallels have varying depth due to the overlap from the increased FoV of the ACS camera. In COSMOS and EGS, most of the area has a three orbit depth with a  $5\sigma$  sensitivity of  $\text{mag}_{\text{F435W}} = 28$ , while the overlap region has a six orbit depth and a sensitivity of  $\text{mag}_{\text{F435W}} = 28.4$ . The GOODS fields already have  $B$ -band coverage of sufficient coverage ( $\text{mag}_{\text{F435W}} \sim 28$ ), so the additional F435W data were

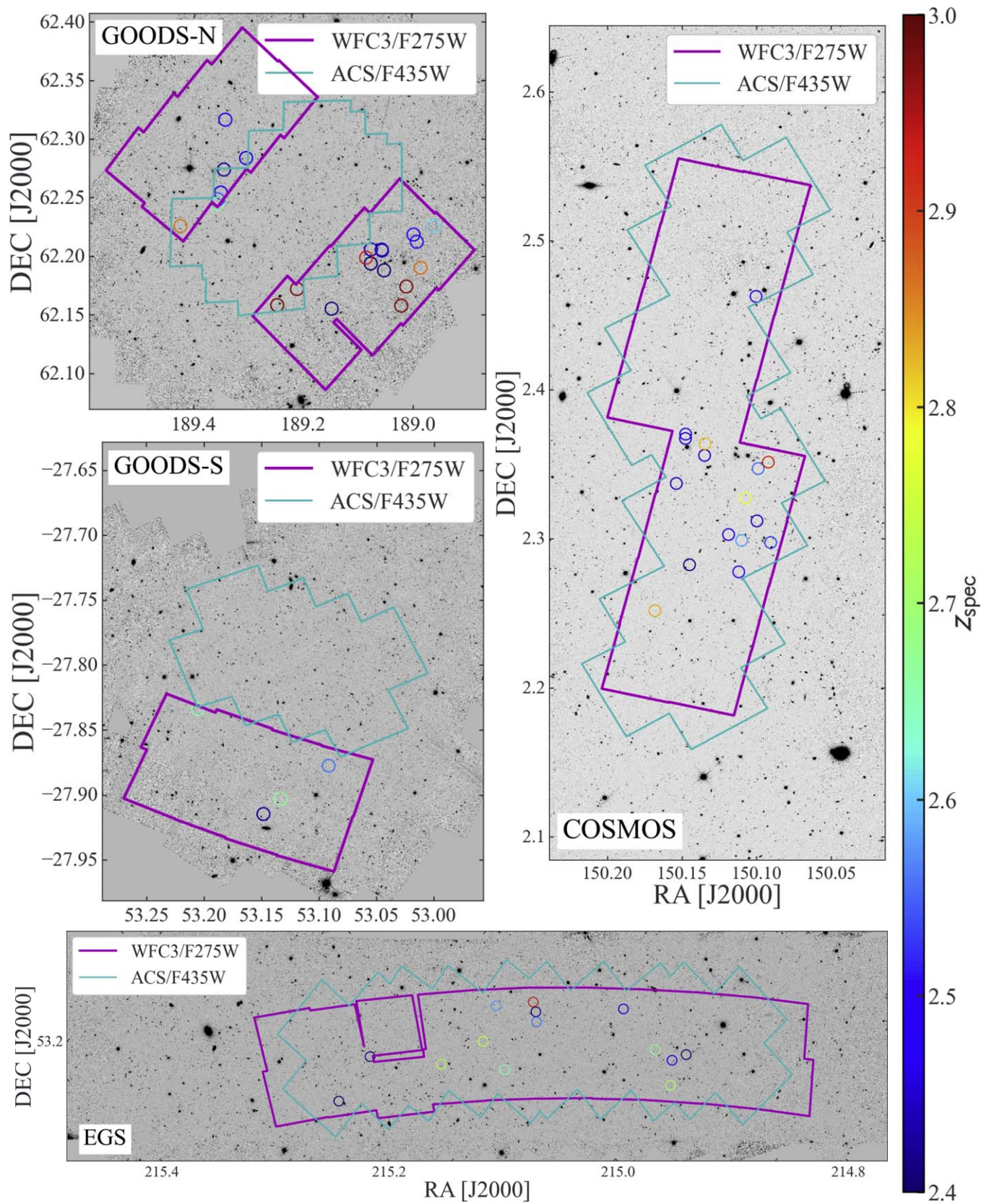


**Figure 1.** The UVCANDELS survey footprints overlaid on top of the F814W mosaics of the four premier CANDELS fields: GOODS-N, GOODS-S, EGS, and COSMOS (N. A. Grogin et al. 2011; A. M. Koekemoer et al. 2011). Small chip gaps of the WFC3 and ACS detectors are not shown from the UVCANDELS footprints. We also highlight the galaxies selected for the stacking analysis elaborated in Section 5. They are color-coded in their spectroscopic redshifts visually inspected in Section 4. The same color-coding is utilized in all four panels.

placed in the central CANDELS-Deep region, where deep archival UV and near-infrared (NIR) data are available.

UVCANDELS comprised 164 orbits of primary UVIS/F275W with ACS/F435W in parallel. Figure 1 shows the UVCANDELS F275W and F435W footprints overlaid on the CANDELS optical imaging mosaics. Small gaps between individual exposures in the F435W coverage are not shown in the figures. The COSMOS and EGS were targeted for 16 and 20 pointings, respectively (approximately  $2 \times 8$  and  $2 \times 10$ , adjusted for scheduling flexibility), enabling F435W coverage in parallel over most of the UV area. In GOODS-S, UVCANDELS obtained eight pointings, to complete coverage of the field. In GOODS-N, UVCANDELS observed two groups of eight pointings ( $2 \times 4$ ), partially during CVZ and near-CVZ opportunities. The survey design employed a standard dithering pattern of WFC3-UVIS-DITHER-LINE to enable recovery of spatial resolution using ASTRODRIZZLE to create mosaics (see Section 3.2 for more details).

In most cases, each pointing was observed in a single visit to enable robust CR rejection. In a few cases, guide star limitations required splitting observations into two-orbit and one-orbit visits. In three visits, initial observations failed, and reobservations were obtained. One visit in the EGS fields failed after more than 90% of the program had been completed, and so was not reobserved.

### 3.2. HST Data Reduction

The WFC3/UVIS and ACS/WFC images were calibrated using custom routines developed in M. A. Rafelski et al. (2015), L. J. Prichard et al. (2022), and specifically for the UVCANDELS data. In order to correct for radiation damage of the WFC3/UVIS detector over time, the F275W data were corrected with the updated CTE correction algorithm (J. Anderson et al. 2021), which includes reduced noise amplification over previous efforts. These F275W images also include the official improved calibrations after 2021 that include concurrent dark subtraction to reduce the blotchy pattern otherwise observed in WFC3/UVIS images and updated flux calibration to match the latest CALSPEC models, which is especially important in the UV (A. Calamida et al. 2021). We generate custom hot pixel masks using cotemporal darks and a variable threshold as a function of the distance to the readout to ensure a uniform number of hot pixels across the CCDs.<sup>43</sup>

In addition, we flag readout cosmic rays (ROCRs) in the F275W data by identifying CR that fall on the detector after the readout of the amplifiers has begun, which are more apparent with the improved CTE correction code. The ROCRs appear as negative divots in the images due to overcorrection by the CTE code, as the ROCRs land closer to the amplifiers than is recorded. The ROCRs are identified as  $3\sigma$  negative outliers within 5 pixels of the readout direction of cosmic-ray hits identified with AstroDrizzle. These negative pixels have the data quality flags set as bad pixels. Finally, we equalize the background levels on the four amplifiers as their bias level is likely affected by CTE degradation of the overscan regions. This results in clean images with constant background levels.<sup>44</sup>

We also correct for scattered light in the WFC/ACS F435W images likely caused by Earth limb light reflected off the telescope structure (J. Biretta et al. 2003; M. J. Dulude et al. 2010). Each exposure is checked for the existence of a gradient by comparing

<sup>43</sup> [https://github.com/lprichard/HST\\_FLC\\_corrections](https://github.com/lprichard/HST_FLC_corrections)

<sup>44</sup> <https://github.com/bsunnquist/uv-vis-skydarks>

**Table 1**

Values of Some Key ASTRODRIZZLE Parameters Set in Creating the New F275W and F435W Mosaics from UVCANDELS Observations

Parameter	Value
driz_cr_corr	True
driz_combine	True
clean	True
final_wcs	True
final_scale	0.06 (0.03)
final_pixfrac	0.8
final_kernel	square
skymethod	globalmin+match
skysub	True
combine_type	imedian

the left quarter to the right quarter of the image, and a difference threshold of  $5e^-$  is applied to a  $3\sigma$  clipped median. If over the threshold, sources are masked in the image, and the gradient is modeled with the Photutils Background2D module. Afterwards, the background level of the two chips is equalized to the mean level determined from a  $3\sigma$  clipped mean after source masking.<sup>45</sup>

### 3.3. Image Mosaicing

The image registration and stacking pipeline was adapted from the one used in A. Alavi et al. (2014). Briefly, the calibrated, flat fielded WFC3/UVIS and ACS/WFC images were combined with the AstroDrizzle software package (S. Gonzaga 2012). To this end, first, we use the TWEAKREG task in the PyRAF/DrizzlePac package to align the individual calibrated images within every single visit to ensure relative astrometric alignment. We then run the AstroDrizzle pipeline on each visit and align the drizzled output image to the CANDELS astrometric reference grid to correct for the small offset in pointing and rotation from different visits with different guide stars. We performed the alignment on the  $30 \text{ mas pix}^{-1}$  images, with a precision of 0.15 pixel, using unsaturated stars and compact sources. These astrometric solutions are then transferred back to the header of the original calibrated flat fielded data using the TWEAKBACK task in the PYRAF/DrizzlePac package. In the end, all of these aligned calibrated images are drizzled to the same pixel scale of 60 (30) mas matched to the CANDELS reference images for the various fields.<sup>46</sup> Table 1 provides the drizzle parameters that were used. The overall image footprints are shown in Figure 1.

ASTRODRIZZLE removes the background, rejects CR, and corrects input images for geometric distortion. In addition to the science images, ASTRODRIZZLE generates an inverse variance map, which we use later to make weight images and to calculate photometry uncertainties. We apply the additional correction to the weight images to account for the correlated noise following S. Casertano et al. (2000). We make publicly available these image mosaics on Mikulski Archive for Space Telescopes.<sup>47</sup>

## 4. Sample Selections and Spectroscopic Redshifts

The focus of our LyC investigation is to measure or set strict limits on the escape fractions of LyC photons from galaxies at

<sup>45</sup> [https://github.com/bsunnquist/uv-vis-skydarks/blob/master/remove\\_gradients.ipynb](https://github.com/bsunnquist/uv-vis-skydarks/blob/master/remove_gradients.ipynb)

<sup>46</sup> <https://archive.stsci.edu/hlsp/candels>

<sup>47</sup> <https://archive.stsci.edu/hlsp/uv-candels>

redshifts  $z \gtrsim 2.4$ . When the red end of the filter response is below the rest-frame Lyman limit, then detected signal can be interpreted as LyC emission (see, e.g., B. M. Smith et al. 2018, 2020). For this technique to succeed, it is important that the study relies on secure galaxy redshifts. In this section, we discuss the sample selection that enables our search for LyC escape.

#### 4.1. Redshift Catalogs

To achieve precise, uncontaminated LyC flux measurements, we chose galaxies with high-quality and accurate spectroscopic redshifts. To accomplish this, we vetted each spectrum in our spectroscopic sample by eye, then selected only the spectra with the highest score ranks by multiple spectroscopy experts on our team.

Our initial compilation of archival spectral data set comprises the Keck observations conducted by A. J. Barger et al. (2008), L. H. Jones et al. (2018, 2021), the C3R2 survey (D. C. Masters et al. 2019), the COSMOS-Magellan active galactic nucleus (AGN) survey (J. R. Trump et al. 2009), the DEEP2 survey (J. A. Newman et al. 2013), the DEIMOS 10K survey (G. Hasinger et al. 2018), the GOODS Very Large Telescope (VLT)/FORS2 survey (E. Vanzella et al. 2007), the GOODS VLT/VIMOS survey (P. Popesso et al. 2009; I. Balestra et al. 2010), GMASS (J. Kurk et al. 2013), the MOSDEF survey (M. T. Kriek et al. 2015), the MUSE-Wide survey (E. C. Herenz et al. 2017), N. A. Reddy et al. (2006), G. P. Szokoly et al. (2004), TKRS/TKRS2 (G. D. Wirth et al. 2004, 2015), VANDELS (L. Pentericci et al. 2018), VIPERS (B. Garilli et al. 2014), VUDS (O. Le Fèvre et al. 2015), VVDS (O. Le Fèvre 2005), and zCOSMOS (S. J. Lilly et al. 2007).

We also supplement this extensive redshift catalog with additional sources identified in a reanalysis of archival HST NIR grism spectroscopy in the CANDELS fields, acquired by primarily the 3D-HST survey (G. B. Brammer et al. 2012; I. G. Momcheva et al. 2016). This reanalysis is part of a novel initiative dubbed the Complete Hubble Archive for Galaxy Evolution (CHARGE; see, e.g., V. Kokorev et al. 2022). The state-of-the-art Grizli software (G. B. Brammer & J. Matharu 2021) is utilized to conduct uniform reprocessing of all archival HST imaging and slitless spectroscopy in the areas of CANDELS fields contained within our UVCANDELS footprints.<sup>48</sup>

Briefly, Grizli reduces the paired preimaging and grism exposures in five steps.

- A. *Preprocessing the raw WFC3 imaging and grism exposures.* This step includes flat-fielding, relative/absolute astrometric alignment, variable/master sky background removal, satellite trail masking, etc.
- B. *Iterative forward-modeling the full FoV grism exposures at visit level.*
- C. *Obtaining best-fit grism redshift of sources through spectral template synthesis.*
- D. *Refining the full FoV grism models.*
- E. *Extracting the science-enabling products (e.g., 1D/2D grism spectra, emission line maps, etc.) for sources of interest.* During step (C), Grizli calculates a number of goodness-of-fit statistics for the redshift fitting procedure. As in X. Wang et al. (2022b, 2022a), we compiled a list of

galaxies with secure grism redshifts at  $z_{\text{grism}} \gtrsim 2.4$ , when all of the following goodness-of-fit criteria are satisfied:  $\chi^2_{\text{reduced}} < 1.5 \wedge (\Delta z)_{\text{posterior}} / (1 + z_{\text{peak}}) < 0.005 \wedge \text{BIC} > 30$ . Here,  $\chi^2_{\text{reduced}}$  is the reduced  $\chi^2$ ,  $(\Delta z)_{\text{posterior}}$  represents the  $1\sigma$  width of redshift posteriors, and *BIC* stands for the Bayesian information criterion estimated from the template fitting procedure. This provides us additional high-quality grism redshifts that we combine with the previous redshift compilations for the subsequent visual inspection, to select the highest fidelity sample for our stacking analysis. In addition, this coherent reanalysis of all the available archival grism exposures covering the entire UVCANDELS fields provides comprehensive measurements of the nebular emission line properties of our sample galaxies, which help divide the full sample into subgroups (see Section 4.2).

#### 4.2. Visual Inspection and Sample Selection

For our visual inspection, we assigned each spectrum to be visually vetted by at least four reviewers randomly chosen from a group of 13 spectroscopy experts. Each reviewer gave a score to the claimed redshift from the survey catalog, with the following rubric, i.e., 0, reliable; 1, possibly correct; or 2, incorrect. This ranking takes into account the alignment of the observed spectral features to their expected position given the reported redshift in the spectrum, the amount of visible noise, the shape of each line or other spectral feature, the presence of unknown/unexpected spectral lines, the presence of neighbors in the corresponding multiband HST images, and the dropout band from the HST images. After ranking was completed, we separated each spectrum into five redshift quality quintiles, based on their median and average scores, where the first quintile has a median  $< 1$  and average  $< 0.5$ , the second quintile has a median  $< 1$  and average  $< 1$ , the third quintile has a median  $< 2$  and average  $< 1.5$ , the fourth quintile has an average  $< 2$  and median  $< 2$ , and the last quintile has a median  $= 2$  and average  $= 2$ . As a consequence, our first redshift quality quintile has 39 galaxies, second has 59, third has 202, fourth has 19, and fifth has 271. Example figures of galaxies in each quintile are shown in the Appendix A.

In our analysis, we will rely on the most secure redshifts, referring to those in the first, second, and third redshift quality quintiles identified by our reviewers. We base our decision to include the third quintile on experience with the overall high quality of the spectra in CANDELS. In this paper, we focus on the search of the LyC signals from individual leakers and/or stacking analysis using the UVCANDELS WFC3/F275W imaging data. So we trim the high-quality redshift catalog by filtering out all spectra taken outside of the UVCANDELS footprints (we defer the analysis outside the UVCANDELS footprints but within other archival UV imaging to a later work). We identify and exclude potential AGN candidates from the deep Chandra X-ray observations in these CANDELS fields (L.-T. Hsu et al. 2014; K. Nandra et al. 2015; Y. Xue et al. 2016; and D. Kocevski private communication), as we present the stacking analysis of the escaping LyC signals from AGNs in a companion work (B. M. Smith et al. 2024). We also exclude sources that lie in close proximity to detector chip gaps of the UVCANDELS F275W imaging, for complex noise properties due to insufficient dithering.

<sup>48</sup> <https://github.com/gbrammer/grizli>

**Table 2**

Number of Sources with High-quality Spectroscopic Redshifts at  $z \in [2.4, 3.0]$ , Compiled from Our Detailed Efforts Visually Inspecting Publicly Available Archival Spectroscopic Observations (See Section 4.2)

Redshift Bin <sup>a</sup>	Full Sample	Subsample			
		GOLD- $z$ <sup>b</sup>	STRONG-[O II] <sup>c</sup>	FAINT-MUV <sup>d</sup>	LOW- $E(B - V)$ <sup>e</sup>
LOW- $z$	28	12	11	11	13
INTERMEDIATE- $z$	28	7	15	14	19

**Notes.** The entire spectroscopic sample consists of 56 galaxies in total, all of which show nondetections ( $\text{SNR} < 3$ ) in the UVCANDELS F275W imaging data. These 56 galaxies are further separated into two redshift bins to facilitate direct comparison of the LyC escape fraction, given the redshift evolution of the IGM transmission and rest-frame wavelength coverage by F275W. For each redshift bin, we further extract subsamples based on specific physical properties of the galaxies. The stacking analysis is applied to the full samples and subsamples (see Section 5.2).

<sup>a</sup> The LOW- $z$  and INTERMEDIATE- $z$  redshift bins bracket galaxies in the redshift range of  $[2.4, 2.5]$  and  $[2.5, 3.0]$ , with a median redshift of  $z_{\text{median}} = 2.44$  and  $z_{\text{median}} = 2.72$ , respectively, for the full samples.

<sup>b</sup> The GOLD- $z$  subsample includes galaxies with the most secure spectroscopic redshifts, compiled from our visual inspection efforts.

<sup>c</sup> The STRONG-[O II] subsample showing significant [O II] emission with  $\text{SNR}_{[\text{O II}]} \gtrsim 3$ , measured from their archival G141 spectra. These galaxies are considered to be prominent line emitters, highly likely those leaking a copious amount of LyC flux.

<sup>d</sup> The FAINT-MUV subsample refers to galaxies with intrinsically faint absolute UV magnitude of  $M_{\text{UV}} > -20.5$ .

<sup>e</sup> The LOW- $E(B - V)$  subsample corresponds to dust-poor galaxies with  $E(B - V) < 0.2$ .

In the end, we compiled a list of 61 galaxies with high-quality spectroscopic redshifts in the range of  $z \in [2.4, 3.0]$ , based on our dedicated visual inspections of these publicly available spectra. Among these 61 galaxies, five show significant detection of F275W fluxes with a signal-to-noise ratio ( $\text{SNR}$ )  $\geq 3$ , whose detailed multiwavelength photometric measurements are presented in Appendix B. We do not opt to include them in the stacking to avoid stacks dominated and biased by a few sources, which can likely be extreme outliers. All the rest of the 56 galaxies in our high-quality spectroscopic redshift sample show nondetections in F275W, and are analyzed in our stacking analysis elaborated in Section 5.2.

To take into account the rapidly evolving IGM opacity with respect to redshift, we divide the entire 56 galaxies into two redshift samples: the LOW- $z$  bin ( $z \in [2.4, 2.5]$ ) and the INTERMEDIATE- $z$  bin ( $z \in [2.5, 3.0]$ ), consisting of 28 and 28 galaxies, respectively (the “full” samples). Galaxies in the LOW- $z$  bin have their Lyman limit lying closer to the red edge of F275W than sources in the INTERMEDIATE- $z$  bin. Within both redshift bins, we also define four subgroups on which the stacking analysis is performed separately, for the purpose of testing the possible correlation between LyC leakage and galaxy global properties. First and foremost, we classify all the galaxies in the first and second redshift quality quintiles with a median score  $< 1$  and average score  $< 1$  (i.e., at least three out of five inspectors deem this redshift measurement secure) as the GOLD- $z$  subsamples. Then, we refer to the galaxies showing significant detection of [O II] $\lambda 3727, 3730$  (hereafter referred to as [O II]) emission in their WFC3/G141 grism spectra as the strong line emitter subsample, denoted by STRONG-[O II]. Moreover, galaxies with intrinsically faint absolute UV magnitude ( $M_{\text{UV}} > -20.5$ ) are selected to form the FAINT-MUV subsamples. Last but not the least, galaxies with poor dust content ( $E(B - V) < 0.2$ ) are considered to be the LOW- $E(B - V)$  subsamples. In total, we have 10 stacking samples in two mutually exclusive redshift ranges. The breakdown of the number counts for the full samples and subsamples analyzed in our stacking analysis are presented in Table 2.

## 5. Image Stacking and Photometry

In this section, we first introduce the procedures to perform spectral energy distribution (SED) fitting to the stacking sample

in Section 5.1. Then, we describe in detail our methodology of image stacking in Section 5.2. Finally, we present our aperture photometry method of the stacked images in Section 5.3.

### 5.1. SED Fitting to the Stacking Sample

We conduct UV-optimized aperture photometry on the new WFC3/F275W and ACS/F435W UVCANDELS data, following the methodology developed as part of the Hubble Ultra-Deep Field UV analysis (H. I. Teplitz et al. 2013; M. A. Rafelski et al. 2015). This method regards the object optical isophotes as more appropriate apertures for counting UV photons than the isophotes defined in NIR wavelengths. The point-spread function and aperture corrections are then performed to make sure the UV and  $B$ -band fluxes are consistent with the previous measurements at other wavelengths. The detailed description of our UV-optimized aperture photometry method is described in L. Sun et al. (2024).

We perform detailed Bayesian inference of the stellar population properties for all the 56 galaxies in the stacking sample, using the CIGALE software (M. Boquien et al. 2019) to fit their multiwavelength photometric measurements, the majority of which are taken from the public CANDELS photometric catalogs, as published in G. Barro et al. (2019) and M. Stefanon et al. (2017a) for GOODS-N and EGS, respectively. We model the galaxy SFH using the delayed  $\tau$  model via the SFHDE-LAYED module, since the sudden onset of star formation and burst episodes in a, e.g., double-exponential parameterization (i.e., the SFH2EXP module) may be too abrupt when the variation of the SFH may be smoother (M. Boquien et al. 2019; A. C. Carnall et al. 2019). We also verify that the different choices of SFH models have a marginal effect on the estimated  $f_{\text{esc}}$  values, on average by  $\sim 4\%$ . We rely on the BC03 stellar population synthesis models (the BC03 module; G. Bruzual & S. Charlot 2003), the infrared dust models of D. A. Dale et al. (2014), and the D. Calzetti et al. (2000) dust extinction law, during the SED fitting with CIGALE. In particular, we utilize the NEBULAR module and keep the parameter NEBULAR\_F\_ESC freely varying to allow for emission lines in the SED.

### 5.2. Stacking Methodology

Our entire stacking sample consists of 56 galaxies with secure spectroscopic redshifts, all showing nondetections (i.e.,

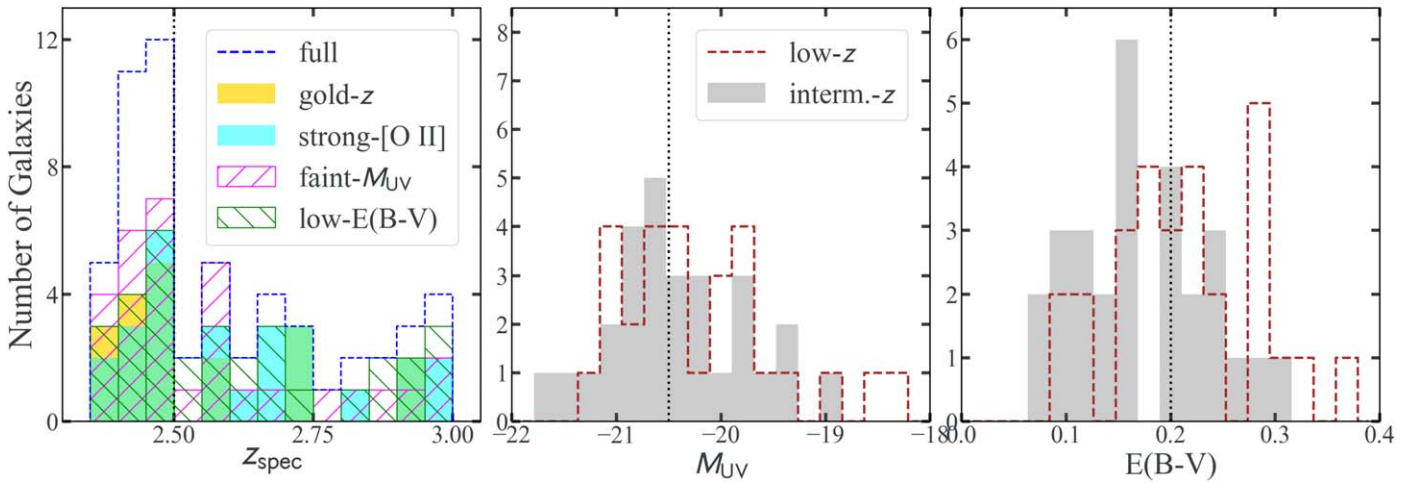


**Figure 2.** Distribution of spectroscopic redshifts ( $z_{\text{spec}}$ ), absolute UV magnitude ( $M_{\text{UV}}$ ), and dust attenuation ( $E(B - V)$ ) of the selected stacking samples. To facilitate direct comparison of the LyC escape fraction, all stacked galaxies are separated into two redshift bins of [2.4,2.5] (LOW-z) and [2.5,3.0] (INTERMEDIATE-z), marked by the black vertical dotted line in the left panel. The black vertical dotted lines in the middle and right panels correspond to the demarcation values of  $M_{\text{UV}} > -20.5$  and  $E(B - V) < 0.2$ , used to compile the FAINT-MUV and LOW-E( $B - V$ ) subsamples, respectively. The numbers counts of the full samples and subsamples within the two redshift bins are broken down in Table 2.

SNR  $< 3$ ) in our UVCANDELS F275W imaging. Following the SED fitting procedures outlined in Section 5.1, we derive the estimates of their absolute UV magnitudes ( $M_{\text{UV}}$ ) and dust attenuation values ( $E(B - V)$ ) shown as the histograms in Figure 2. As given in Table 2, we separate these 56 galaxies into two redshift bins, and obtain in total 10 individual stacking samples, to constrain the LyC escape fraction on a population level, taking into account the rapidly evolving LyC opacity in the IGM (C. C. Steidel et al. 2018; R. Bassett et al. 2021). We adopt the following image stacking procedures, similar to those utilized in B. M. Smith et al. (2018), A. Alavi et al. (2020), and B. M. Smith et al. (2020, 2024). Consistent with the previous studies of LyC leakage that employ stacking procedures, we assume the galaxies selected in our sample to be self-similar, thus allowing us to stack them to make a more accurate measurement of the faint LyC flux.

1. We first make large cutout image stamps in multiple filters (F275W and F435W from our work described in Section 3.3, F606W and F814W from CANDELS) with the size  $10'' \times 10''$  on  $0''.03$  plate scale, centered on each galaxy with a secure spectroscopic redshift that passes our visual vetting described in 4.2. We choose the coadded mosaics on  $0''.03$  plate scale to take full advantage of the high resolution of HST imaging. Yet note that at this stage the object coordinates (R.A. and decl.) are taken from the CANDELS/UVCANDELS multiwavelength photometric catalogs that use  $H_{160}$ -band mosaics as the detection image (Y. Guo et al. 2013; H. Nayyeri et al. 2017; M. Stefanon et al. 2017b; G. Barro et al. 2019). The light centroids measured in F160W and optical/UV filters often do not align, as they probe the rest-frame optical and UV wavelength ranges of our sources of interest.
2. To properly recentroid the optical/UV image cutouts before stacking and at the same time mask possible neighboring contaminants, we utilize the Photutils software to perform photometry on these cutout images. We produce the white-light image from the image cutouts in all available filters weighted by filter mean flux density

(i.e.,  $f_i$ , the PHOTFNU keyword), which is taken as the detection image. We mask regions of pixels in the image cutouts according to existing object isophotes already defined in the  $H_{160}$ -band segmentation maps from the CANDELS photometry.

3. After obtaining the segmentation map from the detection white-light image cutout, we measure the isophotal fluxes associated with each of the segmentation regions in the individual filter image cutouts using Photutils, and select the region that has the brightest F606W flux, under the assumption that the ionizing radiation emerges from the areas dominated by the emission from young massive stars. This is critical in pinpointing the centroid of our galaxies' rest-frame UV light, where the LyC signal most likely originates.
4. We then make small cutout image stamps with  $5'' \times 5''$ , appropriately centered on the object's peak  $V_{606}$ -band flux (corresponding to object's UV-light-weighted centroid), with all contaminants masked. Figure 3 demonstrates the entire procedures for our recentroiding and masking strategy. We also estimate the local sky background and remove that from the SCI extension before stacking. We exclude all surrounding objects outside a certain circular aperture of  $0''.5$ .
5. To combine the surface brightness signals from small cutout image stamps of individual objects, we adopt the UV luminosity ( $L_{\text{UV}}$ ) normalization, described by

$$\begin{aligned} \bar{f} &= \frac{\Sigma(f_i / L_{\text{UV}}^i)}{N_{\text{obj}}} \cdot L_{\text{UV}}^{\text{median}}, \\ \sigma^2 &= \frac{\Sigma(\sigma_i / L_{\text{UV}}^i)^2}{N_{\text{obj}}} \cdot (L_{\text{UV}}^{\text{median}})^2, \end{aligned} \quad (1)$$

where  $f_i$  and  $\sigma_i$  stand for the flux and uncertainty of the  $i$ th source among the entire number of  $N_{\text{obj}}$  that contribute to the stacks.  $L_{\text{UV}}^i$  represents the galaxy rest-frame UV luminosity converted from  $M_{\text{UV}}$  shown in Figure 2.  $\bar{f}$  and  $\sigma$  thus denote the stacked flux and uncertainty.

Equation (1) normalizes galaxy multiband photometry before stacking as the LyC escape fraction is a

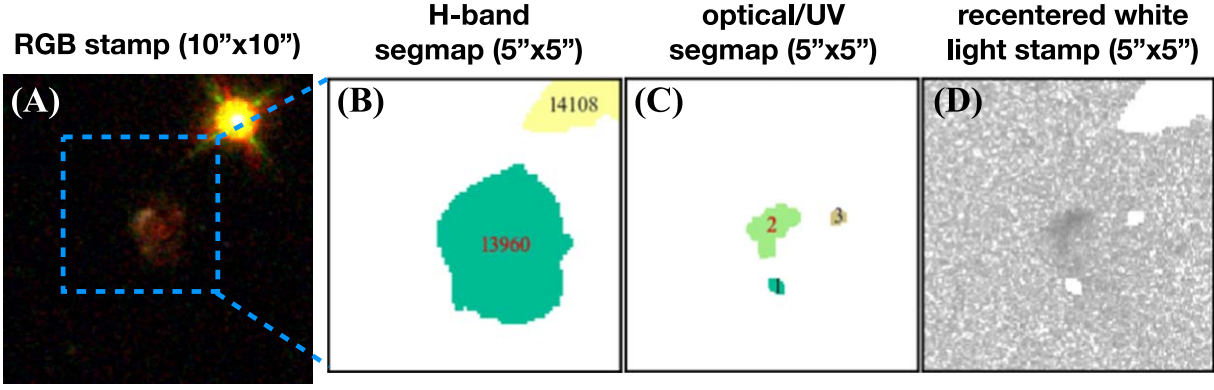


**Figure 3.** An illustration of our recentroiding and contaminant-masking methodology via performing stamp photometry before the stacking analysis. (A) galaxy color-composite stamp with size  $10'' \times 10''$  made from the CANDELS near-infrared and optical imaging, centered on the F160W light centroid. The blue dashed square ( $5'' \times 5''$ ) marks the spatial extent of panels (B)–(D), which are all the same. (B) CANDELS F160W segmentation map defined using the hot+cold source detection scheme (see, e.g., Y. Guo et al. 2013). The ID of our source of interest is marked in red, while the ID of a neighboring source (a star spike) in black. (C) Optical/UV segmentation map using the white-light image as detection image, while masking all neighboring sources. The region #2 has the brightest optical flux, so the light centroid of region #2 is used to recenter panels (B)–(D). (D) The white-light image stamp with neighboring sources and segmented regions within our source of interest (i.e., regions #1 and #3) masked. Here, we clearly see that the light centroids of optical/UV and near-infrared bands do not overlap. These possible offsets can be effectively accounted for using our recentroiding and contaminant-masking methodology.

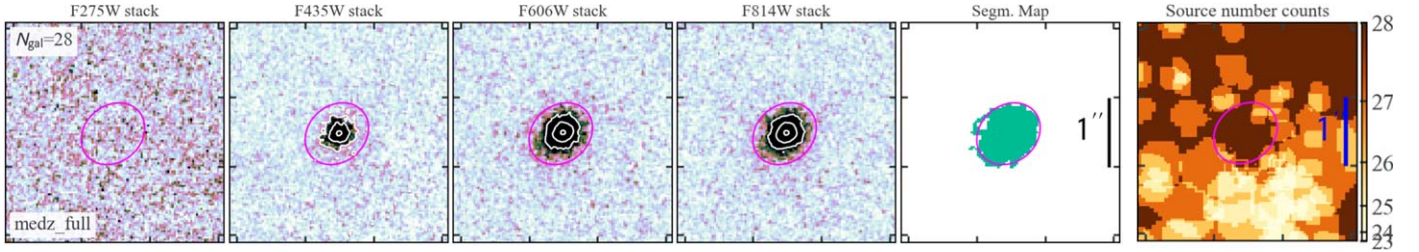


**Figure 4.** The multiband stacked images and the segmentation map utilized for photometric measurements of the full INTERMEDIATE- $z$  galaxy sample in the redshift range of  $z \in [2.5, 3.0]$ . Left five panels: the stacked flux stamps in filters F275W, F435W, F606W, and F814W, created using the  $L_{UV}$  normalization prescribed in Equation (1). The fifth panel from the left shows the segmentation region defined using the F606W stack as detection image, where we derive the isophotal flux in each stack (see Section 5.3 for more details). All stamps have  $3'' \times 3''$  and a plate scale of  $0''.03$ . The magenta ellipse overlaid marks the Kron elliptical aperture (R. G. Kron 1980), matching very well the F606W isophot. The white contours overlaid in the non-LyC filters correspond to the 10th, 30th, and 90th percentiles of the peak flux in respective filters, to highlight the good performance of our recentroiding procedure elaborated in Section 5.2. Rightmost panel: the number count map showing the number of individual sources contributing to each one of the spatial pixels. The number reaches 28 in the center indicating a good recentroiding process before the stacking. The deficit in the outskirts of the source count map comes from masked nearby neighbors of individual galaxies.

relative quantity (F. Marchi et al. 2017; C. C. Steidel et al. 2018). In Section 6, we show results obtained from this stacking method.

- Finally, we apply the  $L_{UV}$  normalization to all galaxy samples listed in Table 2. The large spatial coverage of the UVCANDELS survey presents us an ideal opportunity of testing the strengths of escaping LyC signals as a function of galaxy global properties with sufficient sample statistics. The stacked images in multiple filters for the INTERMEDIATE- $z$  full sample consisting of 28 sources are presented in Figure 4.

### 5.3. Photometry on Image Stacks

Before the image stacking detailed in Section 5.2, we have already subtracted a constant from each cutout image stamp in each filter (F275W, F435W, F606W, and F814W) of each galaxy selected for stacking, to ensure that the mode of the local sky background of each galaxy is achromatically as close to zero as possible. Just in case there still remains some residual sky background signals that survive our stacking procedures, we perform another round of background estimation and removal before the photometry of stacked images. We apply a circular mask with a radius of 45 pixels (i.e.,  $1''.35$ ) to the

central regions of the stacked images in each filter, and bin the unmasked background pixels according to the Freedman–Diaconis rule, following B. M. Smith et al. (2018, 2020). Then, we derive the mode value of the resultant count-rate histogram of these surrounding pixels outside the central masked regions, as the remaining sky background in the stacked images. After subtracting off this remaining background, we make sure that the empty regions of our stacked images only contain random noise.

The sample median redshifts are given in Table 3. At these redshifts, the broadband F606W filter probes the bulk of the rest-frame  $1500 \text{ \AA}$  wavelength regime of source spectrum, conventionally regarded as the UV continuum (UVC). The escaping LyC signals are believed to originate from young star clusters comprising hot, massive O-type stars, which also dominate the blue-UV wavelength range of the host galaxy's SED (see, e.g., E. Vanzella et al. 2022). We therefore take the stacked F606W image as the detection image to define the segmentation map for flux measurements as shown in Figure 4. Following the practice presented in Section 5.2, we utilize the Photutils software to measure the isophotal fluxes in the stacked images in all four filters: F275W, F435W, F606W, and F814W. We adopt the following parameters for Photutils: `detect_thresh = 1`, `analysis_thresh = 1`, `detect_minarea = 8`, `deblend_nthresh = 32`,

**Table 3**  
Measured Photometry and Physical Properties of the Selected Galaxy Samples from Our Stacking Analyses Using  $L_{UV}$  Normalization

Redshift Bin	Sample	$N_{\text{gal}}$	$z_{\text{median}}^{\text{a}}$	Photometric Measurements from the Stacked Images <sup>b</sup>					Measured Physical Properties					
				mag <sub>F275W</sub>	mag <sub>F435W</sub>	mag <sub>F606W</sub>	mag <sub>F814W</sub>	$\left(\frac{F_{\text{LyC}}}{F_{\text{UVC}}}\right)_{\text{obs}}^{\text{c}}$	$M_{\text{UV}}$	$E(B - V)$	$\left(\frac{F_{\text{UVC}}}{F_{\text{LyC}}}\right)_{\text{int}}^{\text{d}}$	$\langle \bar{\tau}_{\text{IGM}} \rangle^{\text{e}}$ (%)	$f_{\text{esc}}^{\text{rel}}$ (%)	$f_{\text{esc}}^{\text{abs}}$ (%)
LOW- $z$	full	28	2.44	>28.70	25.44	24.74	24.46	<0.026	-20.41	0.21	5.06	36.5 [30.0, 42.9]	<36.8	<5.0
LOW- $z$	goldz	12	2.45	>28.99	25.13	24.59	24.40	<0.017	-20.57	0.19	4.98	37.0 [27.1, 46.8]	<23.7	<3.7
LOW- $z$	snO II	11	2.46	>28.66	25.23	24.59	24.45	<0.024	-20.54	0.21	4.58	35.7 [25.6, 45.9]	<32.6	<4.4
LOW- $z$	hiMuv	17	2.44	>28.71	26.11	25.27	24.90	<0.042	-19.88	0.24	6.11	36.9 [28.5, 45.1]	<71.1	<7.1
LOW- $z$	lowEbv	13	2.44	>28.50	25.02	24.49	24.42	<0.025	-20.68	0.16	4.58	36.6 [27.1, 46.1]	<32.4	<7.0
INTERMEDIATE- $z$	full	28	2.72	>28.61	25.84	25.04	24.80	<0.037	-20.52	0.15	6.07	20.0 [14.5, 25.6]	<113.1	<26.1
INTERMEDIATE- $z$	goldz	7	2.73	>28.01	25.42	24.68	24.51	<0.046	-20.84	0.23	6.82	20.2 [8.9, 31.4]	<201.1	<22.5
INTERMEDIATE- $z$	snO II	15	2.71	>28.21	25.58	24.80	24.66	<0.043	-20.73	0.16	6.00	20.1 [12.5, 27.6]	<133.6	<29.0
INTERMEDIATE- $z$	hiMuv	14	2.64	>28.73	26.56	25.67	25.34	<0.059	-19.92	0.18	6.46	22.0 [13.7, 30.2]	<193.6	<35.4
INTERMEDIATE- $z$	lowEbv	19	2.68	>28.47	25.60	24.97	24.82	<0.040	-20.60	0.14	5.86	20.3 [13.4, 27.0]	<117.5	<32.5

**Notes.**

<sup>a</sup> Sample median redshift.

<sup>b</sup> Measurements and  $1\sigma$  limits for the isophotal magnitudes and flux ratios derived from the stacked image stamps. The magnitudes are in unit of ABmag.

<sup>c</sup> The  $1\sigma$  upper limits of the observed ratio of the escaping LyC flux vs. the UVC flux, measured from the empty aperture analysis performed on the stacked F275W images (see Section 6). For each stack, we take the 84.13th percentile of the distribution resulting from the empty aperture analysis as the  $1\sigma$  upper limit reported here, following N. Gehrels (1986).

<sup>d</sup> The intrinsic ratio of the UVC and LyC flux. We compute this ratio for each galaxy within the stacking samples based on their best-fit intrinsic SED and take the median of the distribution as the intrinsic ratio for stacks, listed here.

<sup>e</sup> The mean IGM transmission and  $1\sigma$  confidence interval drawn from the average IGM transmission distribution of all galaxies in the respective stacks. We simulate 10,000 sightlines for each galaxy using the TAOIST\_MC Monte Carlo line-of-sight IGM code (R. Bassett et al. 2021), to account for the high stochasticity of IGM transmission (see Figure 5).

<sup>f</sup> The  $1\sigma$  upper limits of the relative and absolute escape fractions, calculated using 3000 bootstrap random draws from the mean IGM transmission distribution of each stack and 3000 observed LyC-to-UVC flux ratios measured from the empty aperture analysis of each stack. We adopt  $f_{\text{esc}}^{\text{abs}} = f_{\text{esc}}^{\text{rel}} 10^{-0.4 A_{\text{UV}}}$ , where  $A_{\text{UV}} = 10.33 E(B - V)$  is the D. Calzetti et al. (2000) dust reddening law. For each stack, we take the 84.13th percentiles of the resulting histograms of  $f_{\text{esc}}^{\text{rel}}$  and  $f_{\text{esc}}^{\text{abs}}$  as their  $1\sigma$  upper limits reported here, following N. Gehrels (1986).

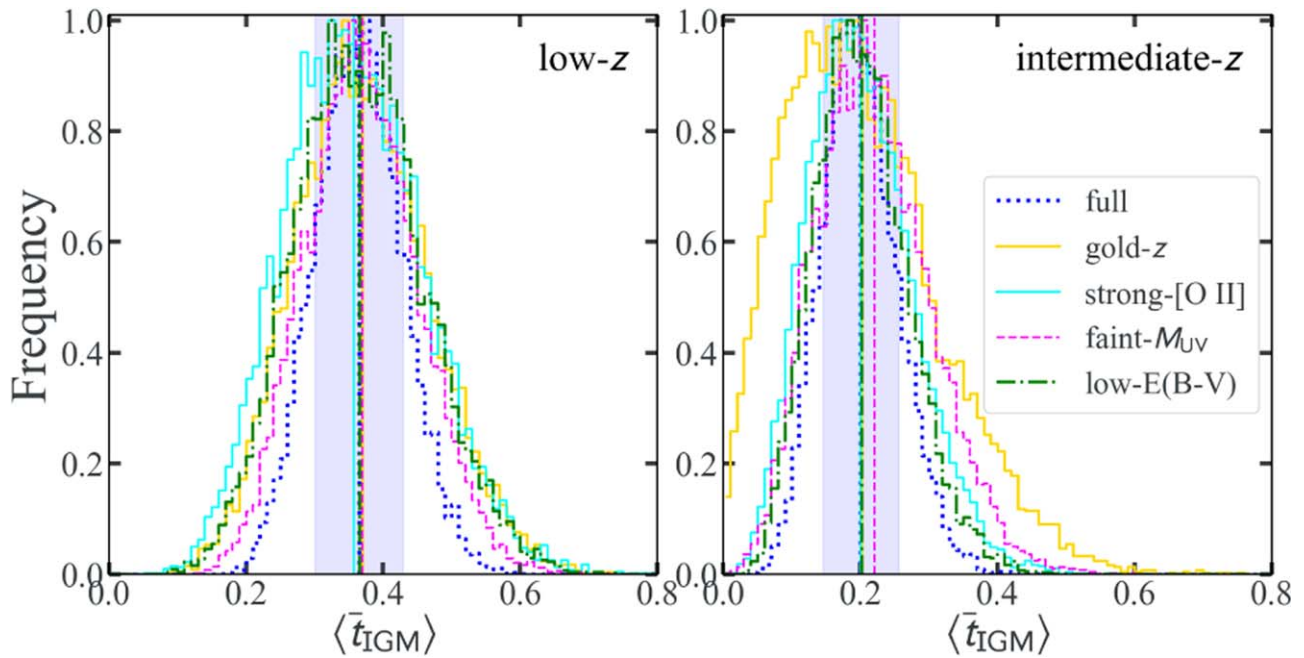


**Figure 5.** Mean IGM transmission distributions for each galaxy sample in the two redshift bins: LOW- $z$  and INTERMEDIATE- $z$  shown in the left and right panels, respectively. In both panels, we show the mean IGM transmission histogram averaged from the full sample in blue dotted lines, with the histograms for the four subsamples represented in other lines. The vertical straight lines correspond to the median values for each histogram, and the blue shaded region marks the  $1\sigma$  range for the full sample. We see that averaging the IGM transmission values randomly drawn from bimodal distributions for a relatively large sample of galaxies at similar redshifts lead to a single-peaked mean IGM transmission distribution, useful for breaking the degeneracy between  $t_{\text{IGM}}$  and the  $f_{\text{esc}}$  inference for the galaxy sample (R. P. Naidu et al. 2018; R. Bassett et al. 2021).

deblend\_mincont = 0.001. Photutils reports the sum of fluxes within the F606W isophote for all four filters. Finally, using the up-to-date zero-points of these four filters, we convert the measured fluxes into isophotal magnitudes given in Table 3. After averaging the best-fit CIGALE SEDs as discussed above, we find an insignificant red-leak of flux into the F275W filter redward of the 912 Å Lyman break of  $\sim 0.8\%$ .

## 6. Inference of the LyC Escape Fraction

In this section, we present the main results from our detailed stacking analysis. Following the standard nomenclature (e.g., C. C. Steidel et al. 2001; B. D. Siana et al. 2010; B. Siana et al. 2015; C. C. Steidel et al. 2018), we define the *relative* escape fraction of LyC as

$$f_{\text{esc}}^{\text{rel}} = \frac{(F_{\text{UVC}}/F_{\text{LyC}})_{\text{int}}}{(F_{\text{UVC}}/F_{\text{LyC}})_{\text{obs}}} \cdot \exp(\tau_{\text{IGM}}), \quad (2)$$

where  $(F_{\text{UVC}}/F_{\text{LyC}})_{\text{int}}$  and  $(F_{\text{UVC}}/F_{\text{LyC}})_{\text{obs}}$  represent the intrinsic and the observed ratios of the UVC and LyC fluxes, respectively, and  $\tau_{\text{IGM}}$  is the IGM opacity. The transmission of the ionizing flux through the intervening IGM (i.e.,  $t_{\text{IGM}} = \exp(-\tau_{\text{IGM}})$ ) is a highly stochastic process, ascribed to its bimodal probability distribution function (PDF). R. Bassett et al. (2021) showed that the PDF of  $t_{\text{IGM}}$  can be depicted by a sudden rise toward  $t_{\text{IGM}} \sim 0$  and a much less prominent second peak at higher values. Due to the strong degeneracy between  $f_{\text{esc}}$  and  $t_{\text{IGM}}$ , the inferred values of  $f_{\text{esc}}$  are often overestimated from the observations of galaxies leaking strong LyC flux under the assumption of a mean  $t_{\text{IGM}}$ , a.k.a. the IGM transmission bias. Fortunately, R. Bassett et al. (2021) verified

that this bias is less fatal for large galaxy ensembles including LyC nondetections.

To determine the appropriate average IGM transmission value for each stack, we use the TAOIST\_MC software (R. Bassett et al. 2021) to generate 10,000 realizations of the line-of-sight IGM transmission models as a function of the observed wavelength per galaxy at its known redshift.<sup>49</sup> We then calculate the filter throughput weighted average of these transmission models for each line of sight using

$$\bar{t}_{\text{IGM}} = \frac{\int \exp(-\tau_{\text{IGM}}) \frac{T_{\text{F275W}}}{\lambda} d\lambda}{\int \frac{T_{\text{F275W}}}{\lambda} d\lambda}, \quad (3)$$

with  $T_{\text{F275W}}$  representing the F275W filter throughput. This ensures that only the observed wavelengths within the F275W filter are considered in the IGM transmission calculations, and any wavelengths outside of the filter would not be used to calculate the average  $f_{\text{esc}}$  of the stack. The result is 56 sets of distributions of 10,000 IGM transmission values through the F275W filter, for the 56 galaxies in the entire redshift range. Then, for any individual stack consisting of  $N_{\text{gal}}$  galaxies, we take the arithmetic mean of the corresponding  $N_{\text{gal}}$  independent IGM transmission values from the respective individual transmission distributions, to obtain the mean IGM transmission, hereafter denoted as  $\langle \bar{t}_{\text{IGM}} \rangle$ , which shows a single-peaked distribution (R. Bassett et al. 2021). In Figure 5, we show the mean IGM transmission distributions for all the 10 stacks. We notice that, in both redshift bins, the mean IGM transmission for the full galaxy sample has the smallest width, as compared to the corresponding subsamples, since the full sample has the

<sup>49</sup> [https://github.com/robbassett/TAOIST\\_MC](https://github.com/robbassett/TAOIST_MC)

largest number of galaxies in each redshift bin. We rely on  $\langle \bar{\tau}_{\text{IGM}} \rangle$  to break the degeneracy between  $t_{\text{IGM}}$  and  $f_{\text{esc}}$ , since the distribution of  $\langle \bar{\tau}_{\text{IGM}} \rangle$  is computed from the Monte Carlo (MC) approach, adequate for our large galaxy samples selected from a wide sky coverage of 426 arcmin<sup>2</sup> in total. The median values and the 1 $\sigma$  error bars corresponding to the [16th, 84th] percentiles are given in Table 3. We perform bootstrap random draws from the  $\langle \bar{\tau}_{\text{IGM}} \rangle$  distribution to derive the constraints on  $f_{\text{esc}}$ , in order to take into account the sample variance of the mean IGM transmission for each stack.

To obtain the appropriate values of the intrinsic flux ratio of UVC to LyC, we run extensive sets of CIGALE SED fitting analysis of all galaxies within the entire stacking samples, following the numerical setup described in Section 5.1. We do not use the observed F275W flux to retrieve model independent intrinsic SED at the LyC wavelengths of all galaxies, adding together the various components (i.e., stellar, nebular lines and continuum, and dust) without IGM and ISM absorption. We then compute the inner products of this intrinsic SED and the filter throughput of F275W and F606W, covering the rest-frame LyC and 1500 Å UVC, respectively, to estimate the intrinsic flux of LyC and UVC for each galaxy in the stacking samples. Finally, we take a median of all the intrinsic UVC to LyC flux ratios of galaxies that reside in each one of the stacks as the sample average  $\left( \frac{F_{\text{UVC}}}{F_{\text{LyC}}} \right)_{\text{int}}$ , shown in Table 3. We note that these intrinsic ratios are consistent with the conventional values quoted in the literature (e.g., L. Guaita et al. 2017; M. J. Rutkowski et al. 2017; B. M. Smith et al. 2018; A. Alavi et al. 2020).

Then, the relative and absolute LyC escape fractions are connected via

$$f_{\text{esc}}^{\text{abs}} = f_{\text{esc}}^{\text{rel}} 10^{-0.4A_{\text{UV}}}, \quad (4)$$

where  $A_{\text{UV}} = 10.33 E(B - V)$  following the Calzetti dust attenuation law (D. Calzetti et al. 2000) appropriate for high- $z$  star-forming galaxies. We take the sample median value of  $E(B - V)$  as the default dust extinction estimates when computing  $f_{\text{esc}}^{\text{abs}}$ . We adopt the  $L_{\text{UV}}$  normalization in stacking described in Equation (1) in Section 5.2. To properly take advantage of our dedicated IGM transmission MC simulations, we perform a bootstrap resample to randomly draw 3000 values from the mean IGM transmission distribution for each stack, in order to incorporate the sample variance in  $\langle \bar{\tau}_{\text{IGM}} \rangle$  in the  $f_{\text{esc}}$  estimates. As a consequence, the measured physical properties for all our stacking galaxy samples are summarized in Table 3. We emphasize that the reported isophotal magnitudes (or upper limits) therein are for a galaxy at the respective median redshift and median  $M_{\text{UV}}$  of the stack.

We first show the stacked image stamps of the INTERMEDIATE- $z$  full sample as an example of the end products from our stacking analyses elaborated in Section 5. The combined images stacked using the  $L_{\text{UV}}$  normalization of all four filters (F275W, F435W, F606W, and F814W) on the entire 3''  $\times$  3'' spatial extent with 0''.03 plate scale are shown in Figure 4. We also exhibit the segmentation map defined in F606W via our Photutils photometry with the default parameters. The 10th, 30th, and 90th percentiles of the peak flux in each non-LyC filter are also marked as white contours. We see that our rigorous stacking methodology ensures a

centrally concentrated light profile in the three non-LyC filters that probe the rest-frame UV spectra of the sample galaxy population. The source number counts as shown in the far right panel of Figure 4 imply a good recentroiding process during stacking.

Our large parent sample size allows us to constrain  $f_{\text{esc}}$  in two separate redshift bins: the LOW- $z$  sample of  $z \in [2.4, 2.5]$  with  $z_{\text{median}} = 2.44$  and the INTERMEDIATE- $z$  sample of  $z \in [2.5, 3.0]$  with  $z_{\text{median}} = 2.72$ , to account for the rapidly evolving IGM opacity across redshifts. Although the full samples of both redshift bins have an equal sample size (i.e., 28 galaxies each), we caution that the derived  $f_{\text{esc}}$  values are not comparable to each other since the F275W filter probes different rest-frame wavelengths. The stacked image stamps of F275W (covering LyC) and F606W (covering the rest-frame 1500 Å flux as UVC) and the segmentation maps for the full samples and subsamples of both redshift bins are shown in Figure 6.

All 10 F275W stacks exhibit nondetection of escaping LyC signals. Consequently, we perform random empty aperture analyses as in L. J. Prichard et al. (2022), to estimate upper limits on the observed ratio of LyC flux to UVC flux. For each of the 10 stacking samples, we randomly draw 3000 Kron elliptical apertures (represented by magenta ellipses in Figure 6) that closely correspond to the F606W isophotes in the nondetection F275W stacked images. We then compute the sum of the fluxes within these apertures, treating them as individual measurements of the F275W isophotal fluxes. This practice provides a range of estimates of the observed LyC/UVC flux ratios for each stack. Following N. Gehrels (1986), we take the 84.13th percentile of this range as the 1 $\sigma$  upper limit on  $\left( \frac{F_{\text{LyC}}}{F_{\text{UVC}}} \right)_{\text{obs}}$ , reported in Table 3. Substituting the 3000 individual measurements of  $\left( \frac{F_{\text{LyC}}}{F_{\text{UVC}}} \right)_{\text{obs}}$  and 3000 bootstrap random draws from the  $\langle \bar{\tau}_{\text{IGM}} \rangle$  distribution shown in Figure 5 into Equation (2) yields a histogram of 3000  $f_{\text{esc}}^{\text{rel}}$  estimates for each stack. The 84.13th percentile of this histogram is adopted as the 1 $\sigma$  upper limit on  $f_{\text{esc}}^{\text{rel}}$  (N. Gehrels 1986). Subsequently, the upper limits on  $f_{\text{esc}}^{\text{abs}}$  are determined using Equation (4). All the upper limits on relative/absolute escape fractions derived from the 10 stacks are reported in Table 3.

We measure a 1 $\sigma$  lower limit of  $\text{mag}_{\text{F275W}} > 28.7$  ABmag and a 1 $\sigma$  upper limit of  $\left( \frac{F_{\text{LyC}}}{F_{\text{UVC}}} \right)_{\text{obs}} < 0.026$  for the LOW- $z$  full sample using the  $L_{\text{UV}}$  normalization. Folding in the sample variance of the mean IGM transmission for the LOW- $z$  full sample, we derive an upper limit of  $f_{\text{esc}}^{\text{rel}} < 36.8\%$  at 1 $\sigma$  confidence level. On average, the LOW- $z$  sample shows slightly higher dust attenuation of  $E(B - V) = 0.21$  than the INTERMEDIATE- $z$  full sample. After correcting for dust, we get a stringent 1 $\sigma$  upper limit of  $f_{\text{esc}}^{\text{abs}} < 5.0\%$  from our 28 galaxies spectroscopically confirmed at  $z \in [2.4, 2.5]$ . We achieve looser 1 $\sigma$  upper limits of  $f_{\text{esc}}^{\text{rel}} < 113.1\%$  and  $f_{\text{esc}}^{\text{abs}} < 26.1\%$  for the INTERMEDIATE- $z$  full sample, partly due to declining IGM transmission at high redshifts, such that  $\langle \bar{\tau}_{\text{IGM}} \rangle$  has a lower median value of  $\sim 20\%$  at  $z \sim 2.7$  than  $\sim 37\%$  at  $z \sim 2.4$ , according to our MC line-of-sight IGM attenuation simulations.

Our large sample size enables us to test the strengths of the escaping LyC flux as a function of galaxy global properties. Within both redshift bins, we further select four subsamples with different criteria defined in Section 4.2. We first repeat our

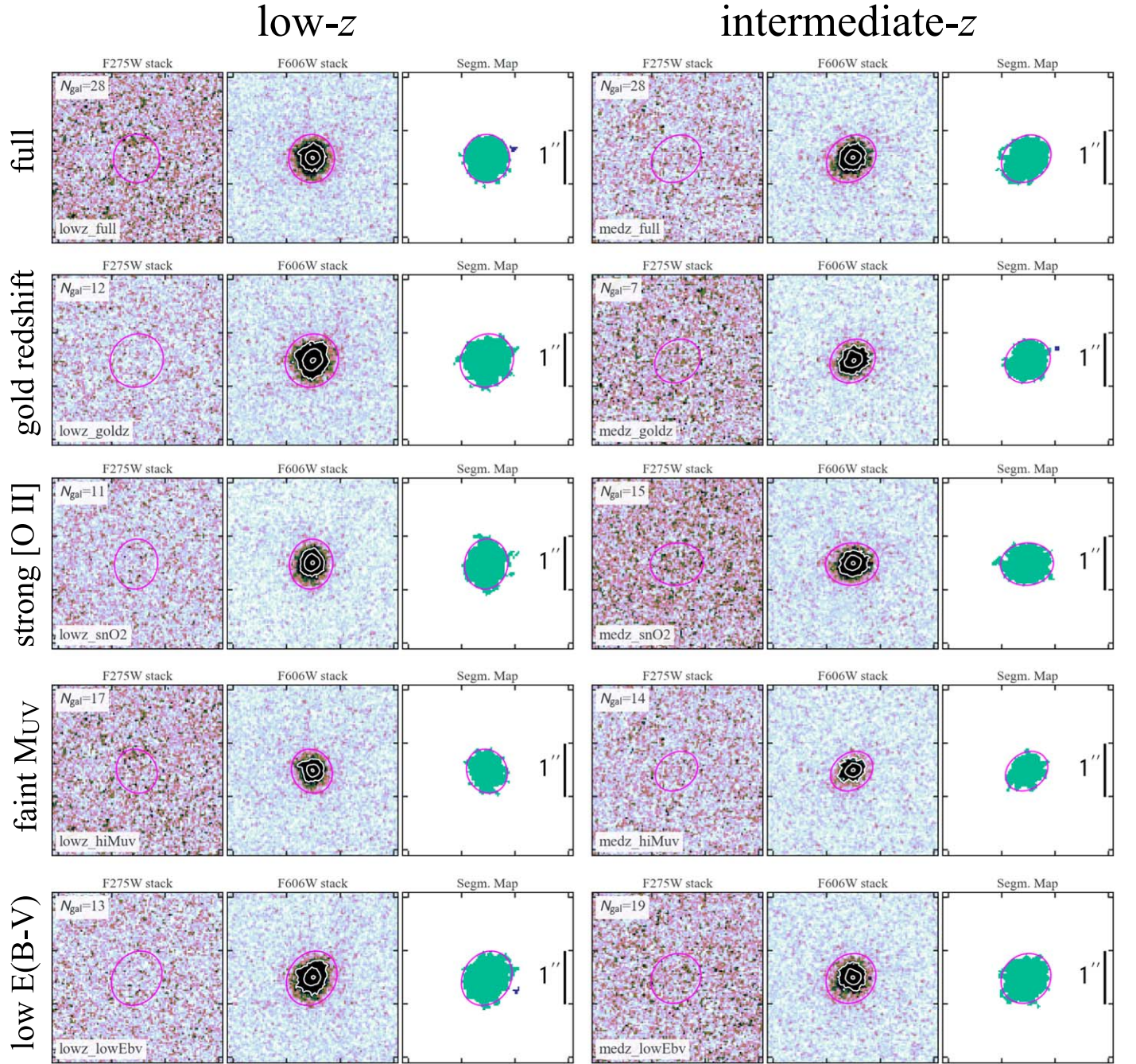


**Figure 6.** LyC and UVC stacks of all the full samples and subsamples separated into two redshift bins: LOW- $z$  (the left three columns) and INTERMEDIATE- $z$  (the right three columns). From top to bottom, the stacking results are shown for the full sample as well as the GOLD- $z$ , STRONG-[O II], FAINT-MUV, LOW- $E(B - V)$  subsamples for each redshift bin. The fluxes of LyC and UVC are covered in filters F275W and F606W respectively. All stacks are created using the  $L_{UV}$  normalization outlined in Equation (1). As in Figure 4, we also show the segmentation map for each stack, where we derive the isophotal fluxes. The magenta ellipse corresponds to the Kron elliptical aperture, which we use to perform the empty aperture analysis to derive upper limits on  $\left(\frac{F_{LyC}}{F_{UVC}}\right)_{obs}$ , since all F275W stacks show nondetections of the escaping LyC signals. The white contours overlaid mark the 10th, 30th, and 90th percentiles of the peak flux for each F606W stack. All stamps share the same size of  $3'' \times 3''$  with a 30 mas plate scale.

stacking analysis on the GOLD- $z$  subsamples, comprising galaxies in the first and second redshift quality quintiles ranked by our dedicated visual inspection efforts, considered to have the most secure spectroscopic redshifts. There are 12 and 7 galaxies in the GOLD- $z$  subsamples in the LOW- $z$  and INTERMEDIATE- $z$  redshift bins, respectively. We achieve a tight  $1\sigma$  upper limit on the observed LyC-to-UVC flux ratio of  $\left(\frac{F_{LyC}}{F_{UVC}}\right)_{obs} < 0.017$  from the LOW- $z$  GOLD- $z$  subsample. This

yields stringent upper limits of  $f_{esc}^{rel} < 23.7\%$  and  $f_{esc}^{abs} < 3.7\%$  at  $1\sigma$  confidence level. The INTERMEDIATE- $z$  GOLD- $z$  subsample produces a comparable  $1\sigma$  upper limit of  $f_{esc}^{abs} < 22.5\%$ , similar to that from the full INTERMEDIATE- $z$  sample.

Next, we perform stacking and photometry on the STRONG-[O II] subsamples. Thanks to the wide coverage of the HST WFC3/G141 slitless spectroscopy in the UVCANDELS fields,

the vast majority of our galaxies have rest-frame near-UV and optical SED measured by G141. The redshift cut imposed by our original sample selection (i.e.,  $z \gtrsim 2.4$ ) precludes our access to some frequently used strong rest-frame optical nebular emission lines, e.g.,  $H\alpha$ , [O III]. The only strong line covered by G141 at this redshift range is [O II]. As such, we take advantage of the CHARGE initiative that reanalyzes all the existing HST NIR imaging and slitless spectroscopy in our fields, to obtain the flux,  $1\sigma$  uncertainty, equivalent width of [O II] for our galaxies, as briefly mentioned in Section 4.2. There are 11 and 15 galaxies in the STRONG-[O II] subsamples in the LOW- $z$  and INTERMEDIATE- $z$  redshift bins, respectively. After incorporating the full distribution of the mean IGM transmission and the observed LyC-to-UVC flux ratio, we obtain the  $1\sigma$  upper limits of  $f_{\text{esc}}^{\text{abs}} < 4.4\%$  and  $f_{\text{esc}}^{\text{abs}} < 29.0\%$  for the LOW- $z$  and INTERMEDIATE- $z$  STRONG-[O II] subsamples, respectively.

Furthermore, we also conduct the stacking analysis to the galaxy subgroups with intrinsically faint  $M_{\text{UV}}$  (the FAINT-MUV subsamples) and the galaxies with low dust extinction (the LOW- $E(B-V)$  subsamples). For the FAINT-MUV subsample selection, we require  $M_{\text{UV}} > -20.5$ , comparable to the characteristic  $M_{\text{UV}}^*$  of the UV luminosity functions at these redshifts (R. J. Bouwens et al. 2022). For the LOW- $E(B-V)$  subsample selection, we require  $E(B-V) < 0.2$ , since dust-rich content is detrimental to the escape of LyC flux. We indeed obtain looser upper limits on the LyC escape fractions from these two subsamples in both redshift bins than those from their corresponding GOLD- $z$  subsamples with equal or less number of sources. Nevertheless, we notice that all our 10 stacks show LyC flux nondetections. These nondetections of F275W flux might stem from the CTE degradation effect. Yet it seems unlikely since the LyC stacks from B. M. Smith et al. (2020) show no evidence of CTE effects when comparing the pristine WFC3/UVIS ERS data (R. A. Windhorst et al. 2011) to the later observed HDUV data (P. A. Oesch et al. 2018), which is more prone to CTE degradation. If assuming the median IGM transmission value for our samples, we get consistent  $1\sigma$  upper limits below  $f_{\text{esc}}^{\text{abs}} < 35\%$  from the 10 samples, generally compatible with some recent findings by I. Jung et al. (2024) at similar redshifts.

## 7. Conclusions

In this paper, we introduce the UVCANDELS HST Cycle-26 Treasury Program (HST-GO-15647, PI: Teplitz), awarded in total 164 orbits of primary WFC3/F275W and coordinated parallel ACS/F435W imaging observations. Its wide sky coverage of  $\sim 426 \text{ arcmin}^2$ , a factor of 2.7 larger than all previous HST UV data combined, makes it the largest space-based UV sky survey of distant galaxies with high angular resolution. We present its first set of science-enabling data products—the coadded imaging mosaics publicly released on the UVCANDELS page<sup>50</sup>—together with an in-depth description of the data reduction procedures. These mosaics are astrometrically aligned to the CANDELS world-coordinate system. The data processing is designed to overcome the issues affecting the quality of UVIS imaging: the CTE degradation, readout cosmic-ray corrections, epoch-varying scattered light during the CVZ observations, etc. As a highlight of the research potential of the UVCANDELS data set, we focus on

one particular application of these imaging mosaics, i.e., searching for strong individual star-forming galaxies that leak LyC radiation and constraining the LyC escape fraction through stacking nondetections.

Our main conclusion is summarized as follows.

1. We build a large compilation of currently existing spectroscopic data sets in the CANDELS fields and organize dedicated visual inspection efforts to vet the quality of the rest-frame UV/optical spectra for sources at  $2.4 \lesssim z \lesssim 3.0$ , to exclude spurious spectroscopic redshift measurements. 56 galaxies with nondetections in F275W (SNR < 3) are selected as the parent stacking sample.
2. We design a rigorous and efficient image stacking methodology using the  $L_{\text{UV}}$  normalization. Our stacking method is capable of properly recentroiding cutout stamps in terms of source optical/UV isophotes, masking any possible neighboring contaminants, and subtracting local residual sky backgrounds.
3. We apply our stacking methodology to galaxies in two separate redshift bins: the LOW- $z$  ( $z \in [2.4, 2.5]$ ) and the INTERMEDIATE- $z$  ( $z \in [2.5, 3.0]$ ) full samples, both consisting of 28 galaxies, respectively. We report no significant ( $>2\sigma$ ) detection of escaping LyC fluxes from both stacks. To properly take into account the highly stochastic IGM attenuation of ionizing radiation, we conduct MC line-of-sight IGM transmission simulations and thus derive the full distribution of the absolute LyC escape fraction. Taking into account the resulting full distributions, we measure the stringent  $1\sigma$  upper limit of  $f_{\text{esc}}^{\text{abs}} \lesssim 5\%$  and  $f_{\text{esc}}^{\text{abs}} \lesssim 26\%$  from the full LOW- $z$  and INTERMEDIATE- $z$  stacks respectively.
4. We further select the galaxies in each redshift bin to get four subsamples according to their global properties, to which we reapply our stacking analysis. All the subsample stacks similarly exhibit nondetection. The stacks at  $z \approx 2.44$  show consistent  $1\sigma$  upper limits below  $f_{\text{esc}}^{\text{abs}} \lesssim 7\%$ , whereas the stacks at  $z \approx 2.72$  show  $f_{\text{esc}}^{\text{abs}} \lesssim 35\%$  at  $1\sigma$  confidence level consistently, after incorporating the full sample variance of mean IGM transmission given by our MC simulations.

As summarized in Section 2, constraining the escape fraction of the ionizing radiation from galaxies and AGNs at  $z \gtrsim 2.4$  (see our companion work of B. M. Smith et al. 2024, for the stacking analysis of AGNs using similar methodology) is merely one of the five major science goals of the UVCANDELS program. The unique UV/optical data set produced and publicly released by the UVCANDELS team will offer tremendous opportunities of scientific explorations on various aspects of galaxy formation and evolution. The science-enabling data products will also support the near and mid-infrared observations from the JWST in these legacy extragalactic survey fields.

## Acknowledgments

We would like to thank the anonymous referee for their very useful comments that helped improve the clarity of this paper. X.W. is supported by the National Natural Science Foundation of China (grant No. 12373009), the CAS Project for Young Scientists in Basic Research grant No. YSBR-062, the Fundamental Research Funds for the Central Universities, the Xiaomi Young Talents Program, and a science research grant

<sup>50</sup> <https://archive.stsci.edu/hlsp/uvcanfels>

from the China Manned Space Project. X.W. acknowledges work carried out, in part, at the Swinburne University of Technology, sponsored by the ACAMAR visiting fellowship, and the hospitality of the International Centre of Supernovae (ICESUN), Yunnan Key Laboratory at Yunnan Observatories, Chinese Academy of Sciences. This work is based on observations with the NASA/ESA Hubble Space Telescope obtained at the Space Telescope Science Institute, which is operated by the Association of Universities for Research in Astronomy, Incorporated, under NASA contract NAS5-26555. Support for program No. HST-GO-15647 was provided through a grant from the STScI under NASA contract NAS5-26555. X.W. acknowledges work carried out, in part, by IPAC at the California Institute of Technology, and was sponsored by the National Aeronautics and Space Administration. R.A.W. acknowledges support from NASA JWST Interdisciplinary Scientist grants NAG5-12460, NNX14AN10G, and 80NSSC18K0200 from GSFC. We thank A. Barger and N. Reddy for providing reduced spectra of their Keck observations, which were useful for our visual inspection efforts. We acknowledge A. Inoue for providing the line-of-sight Monte Carlo IGM transmission code.

*Software:* SExtractor (E. Bertin & S. Arnouts 1996), CIGALE (M. Boquien et al. 2019), Photutils (L. Bradley et al. 2022), Grizli (G. B. Brammer & J. Matharu 2021), AstroDrizzle (W. J. Hack et al. 2021), PyRAF (Science Software Branch at STScI 2012), the line-of-sight Monte Carlo

IGM transmission code by A. K. Inoue et al. (2014), TAOIST\_MC (R. Bassett et al. 2021).

### Appendix A Example Figures Used for Visual Confirmation of Spectroscopic Redshift

As discussed in Section 4.2, we visually confirmed the spectroscopic redshift of the galaxies in our sample since some ground-based spectra are prone to noise and limited by seeing conditions. In Figures A1–A5, we show example figures of galaxies that were ranked into each quintile. The blue curve is the spectrum obtained directly from the archive of the referenced literature source, and the red curve is the same curve convolved with a  $\sigma = 3 \text{ \AA}$  wide Gaussian. Several regions of the spectra where emission/absorption lines are expected are shown in greater detail for inspection of the line profiles. The  $z_{\text{phot}}$  shown is taken from R. E. Skelton et al. (2014). HST image cutouts' filter bands are indicated in their own panels, with the LyC filter distinguished. The original HST mosaics where the image cutouts were extracted from are indicated in blue text below all the image cutouts displayed. The  $\chi^2$  image refers to images constructed as described in A. S. Szalay et al. (1999). Individual ranks are shown for several coauthors, as well as the average, median, and standard deviation of these values.

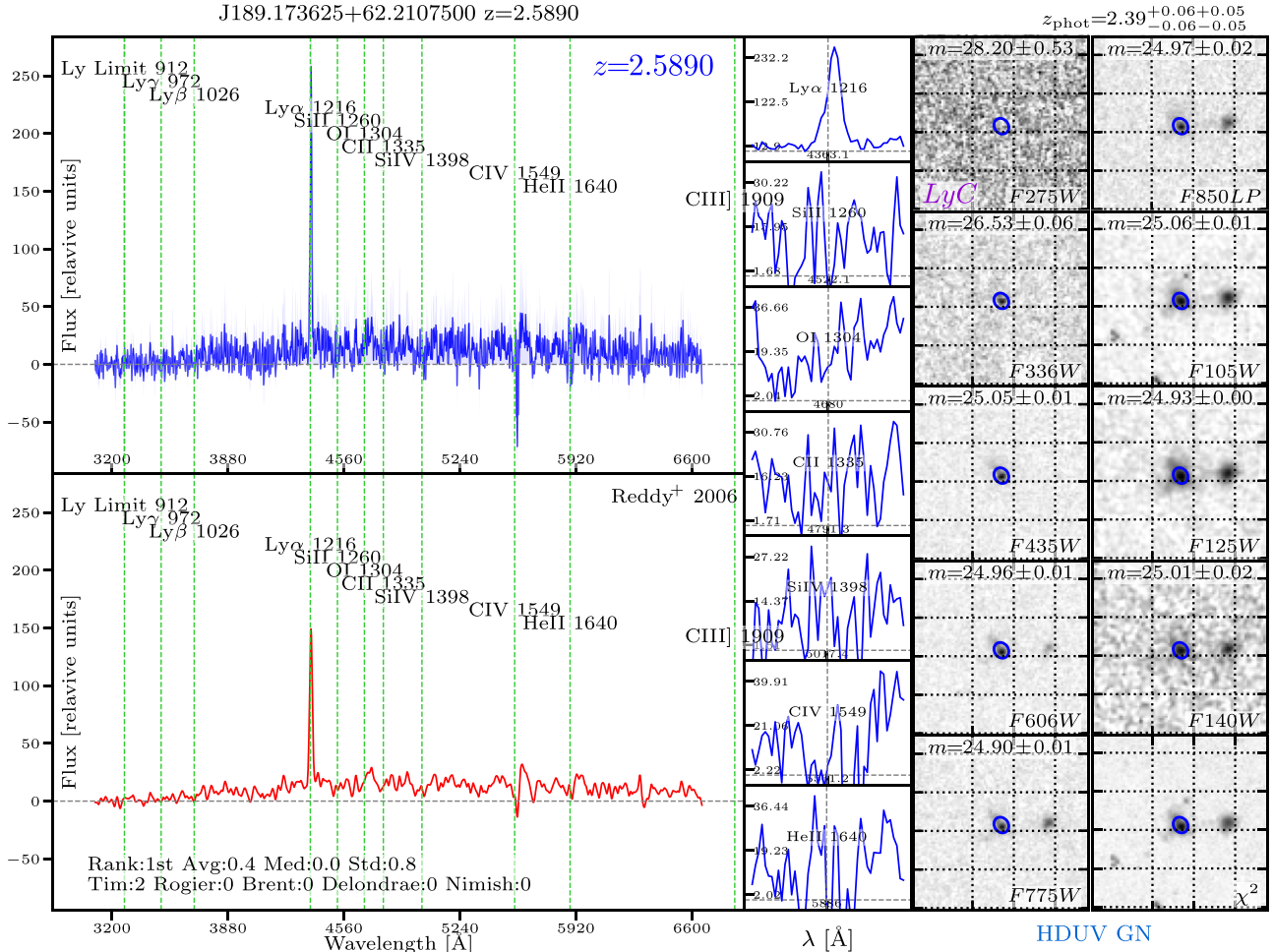
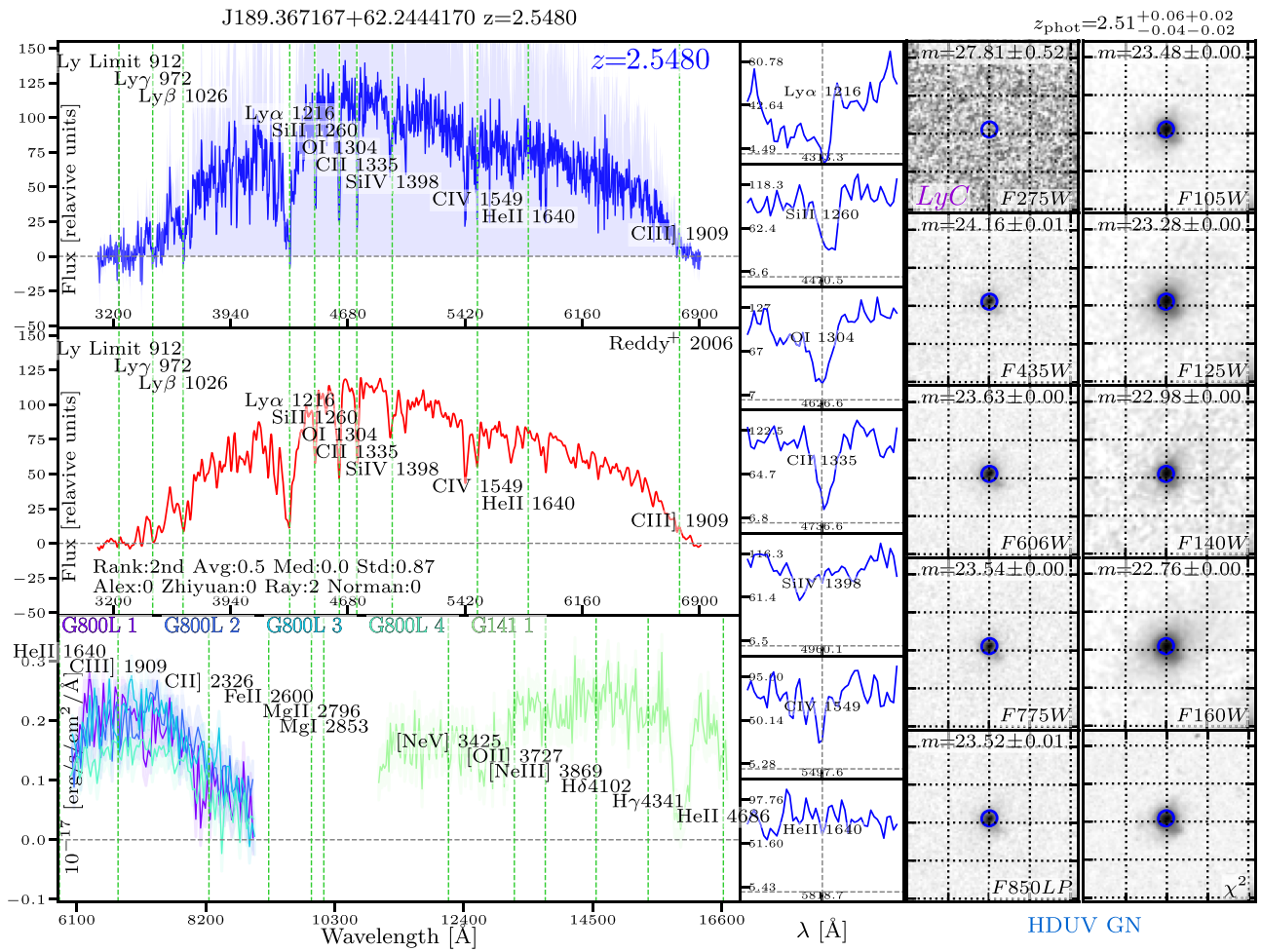


Figure A1. Spectra and images for an example galaxy in the first quintile.



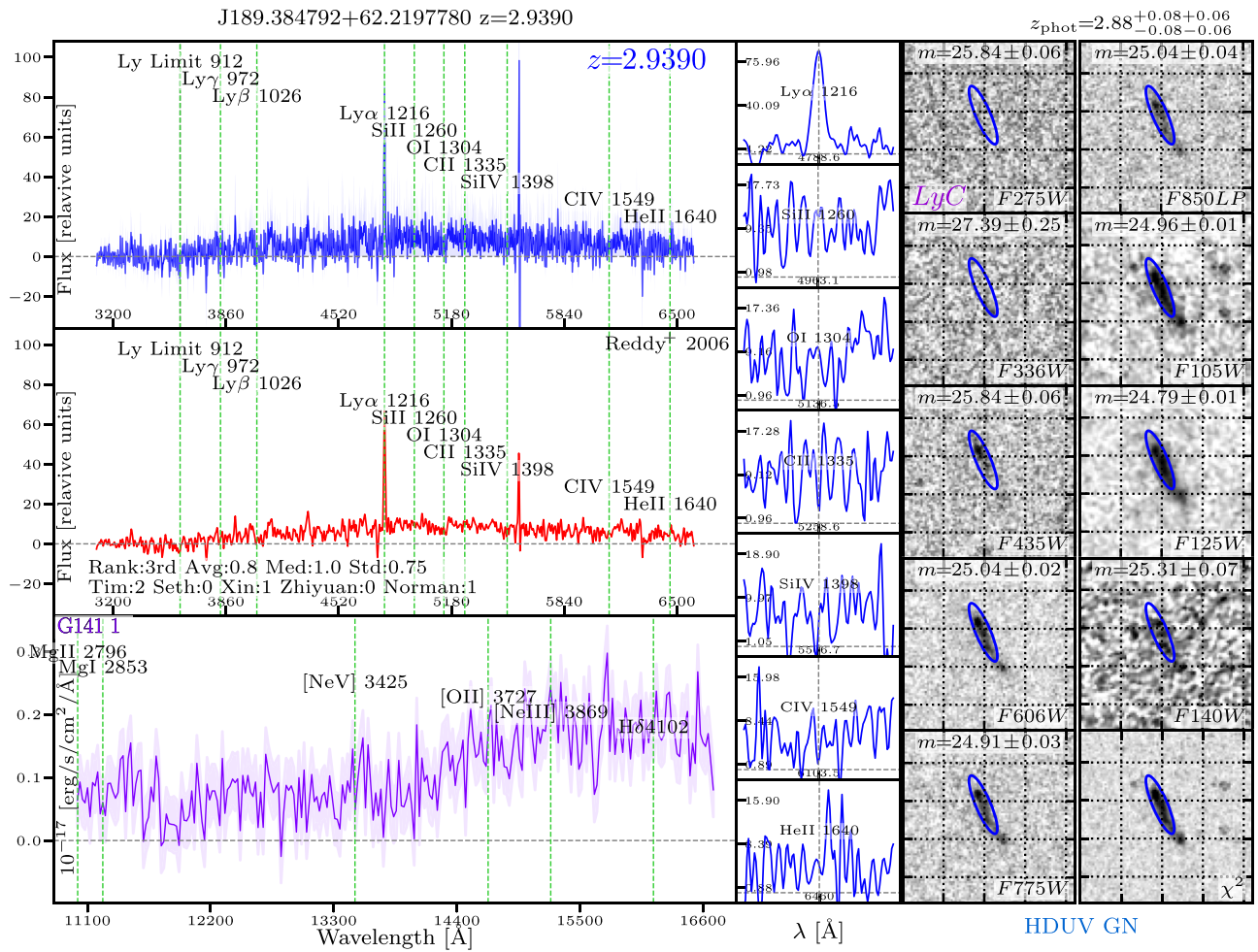


Figure A3. Spectra and images for an example galaxy in the third quintile.

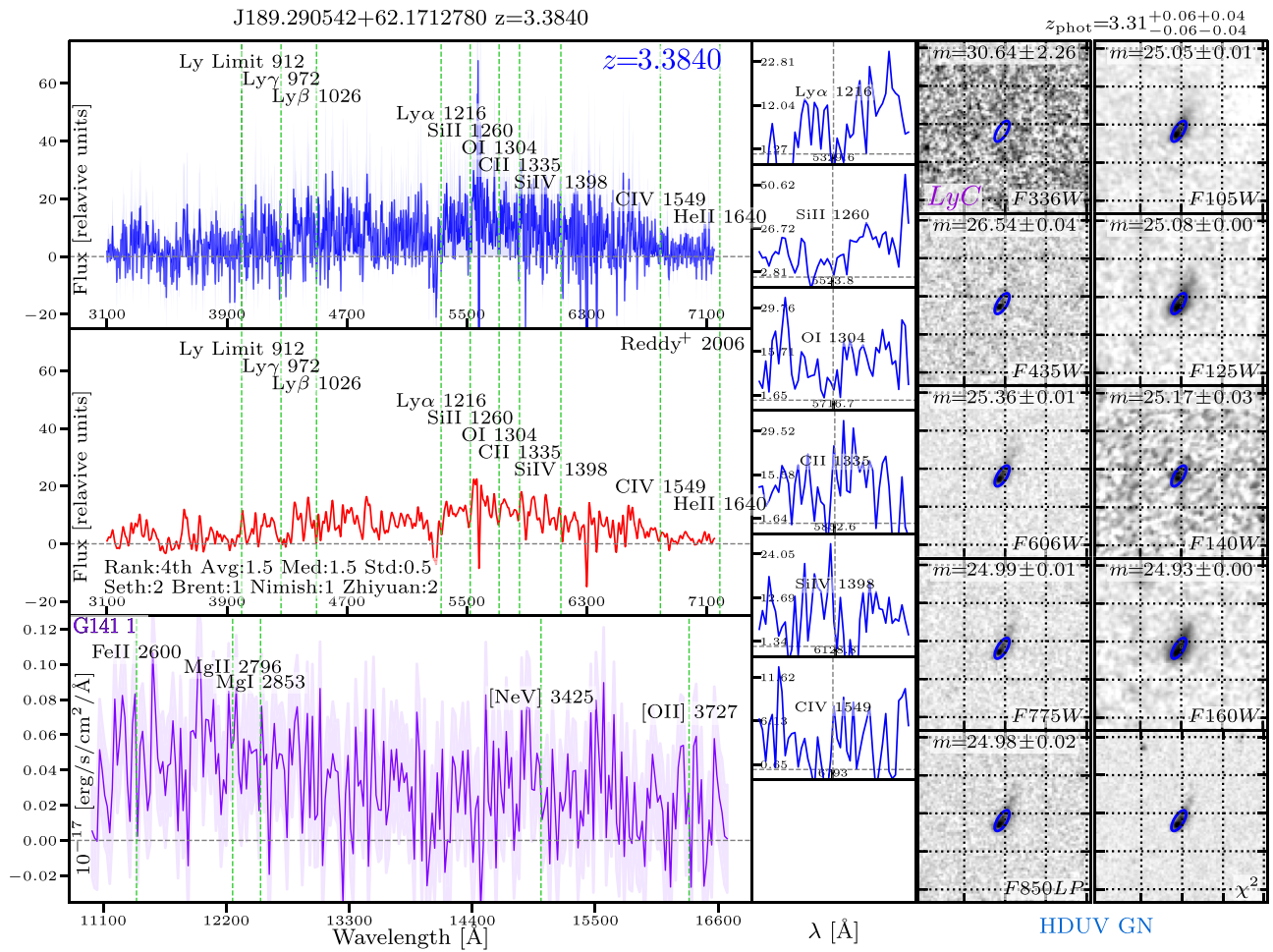


Figure A4. Spectra and images for an example galaxy in the fourth quintile.

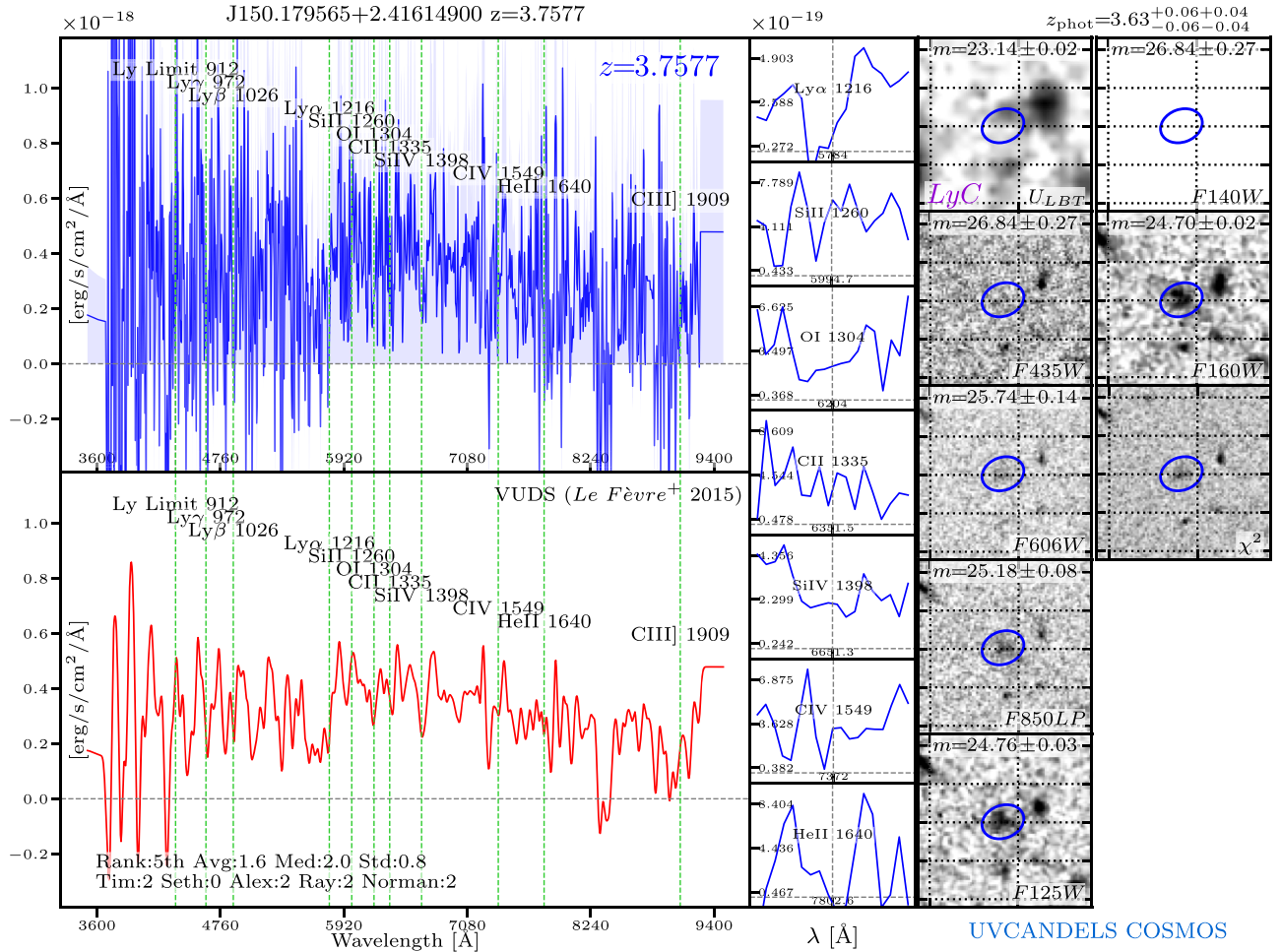


Figure A5. Spectra and images for an example galaxy in the fifth quintile.

## Appendix B

### Individual Galaxies with High-quality $z_{\text{spec}} \geq 2.4$ Showing Significant F275W Detections

In total, five galaxies are identified from the catalog of high-quality spectroscopic redshifts within the UVCANDELS survey footprints, which show relatively strong detection in F275W (e.g.,  $\text{SNR} \geq 3$ ) and in the redshift range of  $z \geq 2.4$ . To ensure that our stacking analysis is not biased by a few sources with bright fluxes, we exclude them in the stacking analysis. In Table 4, we present their multiwavelength photometric

measurements for completeness. We also show the archival spectra taken from ground-based and/or HST grism instruments (A. J. Barger et al. 2008; M. T. Kriek et al. 2015; V. Kokorev et al. 2022) and the HST image stamps of galaxy ID 6226 in Figure B1 as an example. Since GOODS-N is one of the most extensively studied extragalactic fields, there exists a wealth of imaging and spectroscopic data. In particular, the entire field is covered by the deep Keck/MOSFIRE infrared spectroscopy (2 hr each in  $H$  and  $K$  bands) acquired by the MOSDEF program (M. T. Kriek et al. 2015). Furthermore, in

**Table 4**  
Properties of the Five Galaxies Showing Significant WFC3/F275W Flux ( $\text{SNR} \geq 3$ ) from the UVCANDELS Photometric Catalog

Field	ID	R.A. (deg)	Decl. (deg)	$z_{\text{spec}}$	References <sup>a</sup>	HST Photometry (ABmag)						
						F275W	$\text{SNR}_{\text{F275W}}$	F435W	F606W	F814W	F125W	F160W
GOODS-N	00453	189.159046	62.115474	3.656	(1)	26.58	3.0	26.13	24.28	23.98	24.09	23.92
GOODS-N	06226	189.179527	62.185702	3.231	(1), (2), (3)	25.49	5.0	24.52	23.38	23.00	22.70	22.32
GOODS-N	20748	189.378395	62.281930	2.504	(3), (4)	26.35	3.4	25.30	24.61	24.53	23.88	23.44
GOODS-N	22588	189.311919	62.296512	2.486	(1), (4)	25.63	7.2	24.70	24.23	24.17	24.08	24.10
EGS	21708	215.040642	52.995283	2.408	(3)	26.51	3.1	25.60	24.97	24.82	24.31	24.05

**Note.** They all have secure spectroscopic redshifts at  $z \geq 2.4$  confirmed by ground-based and/or HST grism spectroscopy. To ensure that our stacking analysis is not dominated by a few bright sources, we exclude them in our stacking analysis, but present their detailed photometric measurements and spectroscopic redshifts here.  
<sup>a</sup> The references where these spectroscopic redshifts are sourced from: (1) A. J. Barger et al. (2008). (2) CHArGE (V. Kokorev et al. 2022). (3) MOSDEF (M. T. Kriek et al. 2015). (4) N. A. Reddy et al. (2006).

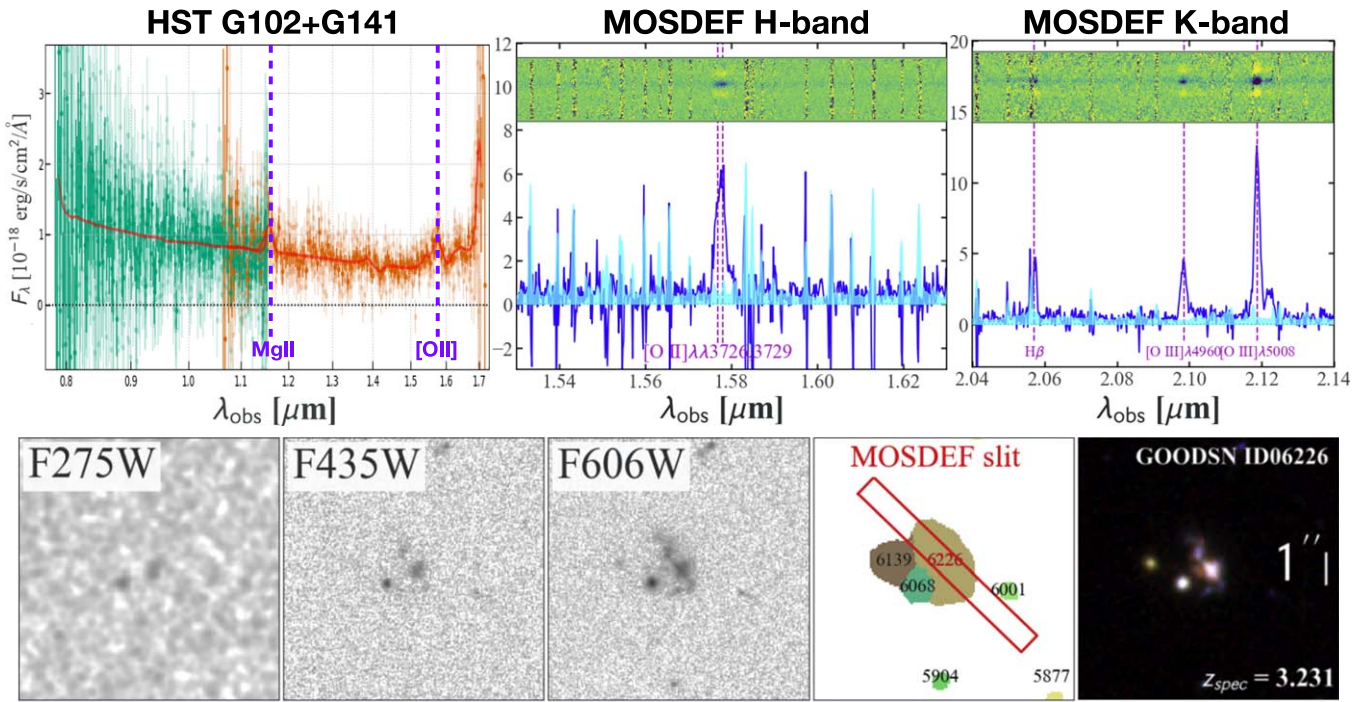


**Figure B1.** Galaxy ID 6226 at  $z = 3.23$  in the GOODS-N field, one example of the five galaxies showing significant F275W detections. Top: the spectra of ID 6226 taken from HST G102+G141 slitless spectroscopy and MOSDEF (in  $H$  and  $K$  bands), showing strong emission features marked by the vertical dashed lines in magenta. The multiple pronounced emission features pinpoint its spectroscopic redshift securely at  $z = 3.23$ . The orientation of the MOSDEF slit is shown in the segmentation map displayed in the bottom row. Bottom: multiwavelength (F275W, F435W, F606W) postage stamps obtained by HST, the F160W segmentation map, and the color-composite image produced from HST imaging. The F275W stamp is smoothed by a boxcar kernel with a width of  $0''.1$  to highlight the detection. This galaxy has  $\text{mag}_{\text{F275W}} = 25.5$  ABmag detected at a high significance of  $5\sigma$ .

the whole field, there also exists HST grism spectroscopy of both G102 (two orbits by HST-GO-13420, PI: Barro) and G141 (two orbits by HST-GO-11600, PI: Weiner). From these existing deep MOSFIRE  $H$ - and  $K$ -band spectroscopy, we see pronounced nebular emission features of [O III],  $H\beta$ , and [O II] lines, with fluxes being  $20.7 \pm 0.3$ ,  $5.4 \pm 0.7$ , and  $9.8 \pm 0.6$  in units of  $10^{-17} \text{ erg}^{-1} \text{ cm}^{-2}$ , respectively. The [O II] and Mg II lines are also clearly detected in HST grism spectroscopy. The wide wavelength coverage ( $0.8\text{--}1.7 \mu\text{m}$ ) of this joint G102-G141 spectroscopy at Hubble's angular resolution basically rules out any possibilities of foreground contamination, since only the spectral features at  $z = 3.23$  are seen. ID06226's F275W magnitude is 25.5 ABmag detected at a  $5\sigma$  significance, and its apparent magnitudes in  $B_{435}$ ,  $V_{606}$ ,  $I_{814}$ ,  $J_{125}$ , and  $H_{160}$  bands are 24.5, 23.4, 23.0, 22.7, and 22.3 ABmag, respectively.

#### ORCID iDs

Xin Wang <https://orcid.org/0000-0002-9373-3865>  
 Harry I. Teplitz <https://orcid.org/0000-0002-7064-5424>  
 Brent M. Smith <https://orcid.org/0000-0002-0648-1699>  
 Rogier A. Windhorst <https://orcid.org/0000-0001-8156-6281>  
 Marc Rafelski <https://orcid.org/0000-0002-9946-4731>  
 Vihang Mehta <https://orcid.org/0000-0001-7166-6035>  
 Anahita Alavi <https://orcid.org/0000-0002-8630-6435>  
 Zhiyuan Ji <https://orcid.org/0000-0001-7673-2257>  
 Gabriel Brammer <https://orcid.org/0000-0003-2680-005X>  
 James Colbert <https://orcid.org/0000-0001-6482-3020>  
 Norman Grogan <https://orcid.org/0000-0001-9440-8872>  
 Nimish P. Hathi <https://orcid.org/0000-0001-6145-5090>

Anton M. Koekemoer <https://orcid.org/0000-0002-6610-2048>  
 Laura Prichard <https://orcid.org/0000-0002-0604-654X>  
 Claudia Scarlata <https://orcid.org/0000-0002-9136-8876>  
 Ben Sunnquist <https://orcid.org/0000-0003-3759-8707>  
 Pablo Arrabal Haro <https://orcid.org/0000-0002-7959-8783>  
 Christopher Conselice <https://orcid.org/0000-0003-1949-7638>  
 Eric Gawiser <https://orcid.org/0000-0003-1530-8713>  
 Yicheng Guo <https://orcid.org/0000-0003-2775-2002>  
 Matthew Hayes <https://orcid.org/0000-0001-8587-218X>  
 Rolf A. Jansen <https://orcid.org/0000-0003-1268-5230>  
 Ray A. Lucas <https://orcid.org/0000-0003-1581-7825>  
 Robert O'Connell <https://orcid.org/0000-0002-8190-7573>  
 Brant Robertson <https://orcid.org/0000-0002-4271-0364>  
 Michael Rutkowski <https://orcid.org/0000-0003-3527-1428>  
 Brian Siana <https://orcid.org/0000-0002-4935-9511>  
 Eros Vanzella <https://orcid.org/0000-0002-5057-135X>  
 Teresa Ashcraft <https://orcid.org/0000-0003-4439-6003>  
 Micaela Bagley <https://orcid.org/0000-0002-9921-9218>  
 Ivano Baronchelli <https://orcid.org/0000-0003-0556-2929>  
 Guillermo Barro <https://orcid.org/0000-0001-6813-875X>  
 Alex Blanche <https://orcid.org/0000-0003-2102-3933>  
 Adam Broussard <https://orcid.org/0000-0002-7767-5044>  
 Timothy Carleton <https://orcid.org/0000-0001-6650-2853>  
 Nima Chartab <https://orcid.org/0000-0003-3691-937X>  
 Yingjie Cheng <https://orcid.org/0000-0001-8551-071X>  
 Alex Codoreanu <https://orcid.org/0000-0001-9560-9174>  
 Seth Cohen <https://orcid.org/0000-0003-3329-1337>  
 Y. Sophia Dai <https://orcid.org/0000-0002-7928-416X>  
 Behnam Darvish <https://orcid.org/0000-0003-4919-9017>  
 Romeel Davé <https://orcid.org/0000-0003-2842-9434>

Laura DeGroot  <https://orcid.org/0000-0001-9022-665X>  
 Duilia De Mello  <https://orcid.org/0000-0003-1624-8425>  
 Mark Dickinson  <https://orcid.org/0000-0001-5414-5131>  
 Najmeh Emami  <https://orcid.org/0000-0003-2047-1689>  
 Henry Ferguson  <https://orcid.org/0000-0001-7113-2738>  
 Leonardo Ferreira  <https://orcid.org/0000-0002-8919-079X>  
 Keely Finkelstein  <https://orcid.org/0000-0003-0792-5877>  
 Steven Finkelstein  <https://orcid.org/0000-0001-8519-1130>  
 Jonathan P. Gardner  <https://orcid.org/0000-0003-2098-9568>  
 Timothy Gburek  <https://orcid.org/0000-0002-7732-9205>  
 Mauro Giavalisco  <https://orcid.org/0000-0002-7831-8751>  
 Andrea Grazian  <https://orcid.org/0000-0002-5688-0663>  
 Caryl Gronwall  <https://orcid.org/0000-0001-6842-2371>  
 Shoubaneh Hemmati  <https://orcid.org/0000-0003-2226-5395>  
 Justin Howell  <https://orcid.org/0000-0002-5924-0629>  
 Kartheik Iyer  <https://orcid.org/0000-0001-9298-3523>  
 Sugata Kaviraj  <https://orcid.org/0000-0002-5601-575X>  
 Peter Kurczynski  <https://orcid.org/0000-0002-8816-5146>  
 Ilin Lazar  <https://orcid.org/0009-0000-1797-0300>  
 John MacKenty  <https://orcid.org/0000-0001-6529-8416>  
 Kameswara Bharadwaj Mantha  <https://orcid.org/0000-0002-6016-300X>  
 Alec Martin  <https://orcid.org/0000-0002-6632-4046>  
 Garreth Martin  <https://orcid.org/0000-0003-2939-8668>  
 Tyler McCabe  <https://orcid.org/0000-0002-5506-3880>  
 Bahram Mobasher  <https://orcid.org/0000-0001-5846-4404>  
 Kalina Nedkova  <https://orcid.org/0000-0001-5294-8002>  
 Charlotte Olsen  <https://orcid.org/0000-0002-8085-7578>  
 Lillian Otteson  <https://orcid.org/0000-0001-9665-3003>  
 Swara Ravindranath  <https://orcid.org/0000-0002-5269-6527>  
 Caleb Redshaw  <https://orcid.org/0000-0002-9961-2984>  
 Zahra Sattari  <https://orcid.org/0000-0002-0364-1159>  
 Emmaris Soto  <https://orcid.org/0000-0002-2390-0584>  
 L. Y. Aaron Yung  <https://orcid.org/0000-0003-3466-035X>  
 Bonnabelle Zabelle  <https://orcid.org/0000-0002-7830-363X>

## References

- Alavi, A., Siana, B. D., Richard, J., et al. 2014, *ApJ*, **780**, 143  
 Alavi, A., Colbert, J. W., Teplitz, H. I., et al. 2020, *ApJL*, **904**, 59  
 Anderson, J., Baggett, S., & Kuhn, B. 2021, Updating the WFC3/UVIS CTE model and Mitigation Strategies, Instrument Science Report 2021-9,  
 Ashcraft, T. A., Windhorst, R. A., Jansen, R. A., et al. 2018, *PASP*, **130**, 064102  
 Atek, H., Labbé, I., Furtak, L. J., et al. 2024, *Natur*, **626**, 975  
 Balestra, I., Mainieri, V., Popesso, P., et al. 2010, *A&A*, **512**, A12  
 Barger, A. J., Cowie, L. L., & Wang, W.-H. 2008, *ApJ*, **689**, 687  
 Barro, G., Prez-Gonzalez, P. G., Cava, A., et al. 2019, *ApJS*, **243**, 22  
 Barros, S. d., Vanzella, E., Amorn, R., et al. 2016, *A&A*, **585**, A51  
 Bassett, R., Ryan-Weber, E. V., Cooke, J., et al. 2021, *MNRAS*, **502**, 108  
 Begley, R., Cullen, F., McLure, R. J., et al. 2022, *MNRAS*, **513**, 3510  
 Bergvall, N., Zackrisson, E., Andersson, B.-G., et al. 2006, *A&A*, **448**, 513  
 Bertin, E., & Arnouts, S. 1996, *A&AS*, **117**, 393  
 Bian, F.-Y., Fan, X., McGreer, I. D., Cai, Z., & Jiang, L.-H. 2017, *ApJ*, **837**, L12  
 Biretta, J., van Orsow, D., Sparks, W., Reinhart, M., & Vick, A. 2003, ACS Background Light vs. Bright Earth Limb Angle, Instrument Science Report ACS 2003-05,  
 Boquien, M., Burgarella, D., Roehly, Y., et al. 2019, *A&A*, **622**, A103  
 Borthakur, S., Heckman, T., Leitherer, C., & Overzier, R. A. 2014, *Sci*, **346**, 216  
 Bouwens, R. J., Illingworth, G., Ellis, R. S., Oesch, P., & Stefanon, M. 2022, *ApJ*, **940**, 55  
 Bradley, L., Sipocz, B., Robitaille, T., et al. 2022, *astropy/Photutils: v1.5.0*, Zenodo, doi:10.5281/zenodo.6825092  
 Brammer, G. B., & Matharu, J. 2021, *grizli v1.3.2*, Zenodo, doi:10.5281/zenodo.5012699  
 Brammer, G. B., Dokkum, P. G. v., Franx, M., et al. 2012, *ApJS*, **200**, 13  
 Bruzual, G., & Charlot, S. 2003, *MNRAS*, **344**, 1000  
 Calamida, A., Mack, J., Medina, J., et al. 2021, New Time-dependent WFC3 UVIS Inverse Sensitivities, Instrument Science Report WFC3 2021-4,  
 Calzetti, D., Armus, L., Bohlin, R. C., et al. 2000, *ApJ*, **533**, 682  
 Carnall, A. C., McLure, R. J., Dunlop, J. S., et al. 2019, arXiv:1903.11082  
 Casertano, S., Mello, D. F. d., Dickinson, M. E., et al. 2000, *AJ*, **120**, 2747  
 Dale, D. A., Helou, G., Magdis, G. E., et al. 2014, *ApJ*, **784**, 83  
 Dayal, P., Volonteri, M., Schneider, R., et al. 2020, *MNRAS*, **495**, 3065  
 Dulude, M. J., Rajan, A., Viana, A., Baggett, S., & Petro, L. 2010, in 2010 STScI Workshop - Hubble after SM4, Preparing JWST, ed. S. Deustua & C. Oliveira (Baltimore, MD: STScI), 62  
 Fan, X., Carilli, C. L., & Keating, B. 2006, *ARA&A*, **44**, 415  
 Finkelstein, S. L., D'Aloisio, A., Paardekooper, J.-P., et al. 2019, *ApJ*, **879**, 36  
 Fletcher, T. J., Tang, M., Robertson, B. E., et al. 2019, *ApJ*, **878**, 87  
 Flury, S. R., Jaskot, A. E., Ferguson, H. C., et al. 2022, *ApJS*, **260**, 1  
 Garilli, B., Guzzo, L., Scodreggio, M., et al. 2014, *A&A*, **562**, A23  
 Gehrels, N. 1986, *ApJ*, **303**, 336  
 Gonzaga, S. 2012, The DrizzlePac Handbook, HST Data Handbook,  
 Grogin, N. A., Kocevski, D. D., Faber, S. M., et al. 2011, *ApJS*, **197**, 35  
 Guaita, L., Talia, M., Pentericci, L., et al. 2017, *A&A*, **606**, A19  
 Guo, Y., Ferguson, H. C., Giavalisco, M., et al. 2013, *ApJS*, **207**, 24  
 Hack, W. J., Cara, M., Sosey, M., et al. 2021, *DrizzlePac v3.3.0*, Zenodo, doi:10.5281/zenodo.5534751  
 Hasinger, G., Capak, P. L., Salvato, M., et al. 2018, *ApJ*, **858**, 77  
 Herenz, E. C., Urrutia, T., Wisotzki, L., et al. 2017, *A&A*, **606**, A12  
 Hsu, L.-T., Salvato, M., Nandra, K., et al. 2014, *ApJ*, **796**, 60  
 Inoue, A. K., Shimizu, I., Iwata, I., & Tanaka, M. 2014, *MNRAS*, **442**, 1805  
 Iwata, I., Inoue, A. K., Matsuda, Y., et al. 2009, *ApJ*, **692**, 1287  
 Izotov, Y. I., Orlitov, I., Schaerer, D., et al. 2016, *Natur*, **529**, 178  
 Izotov, Y. I., Worseck, G., Schaerer, D., et al. 2021, *MNRAS*, **503**, 1734  
 Izotov, Y. I., Worseck, G., Schaerer, D., et al. 2018, *MNRAS*, **478**, 4851  
 Ji, Z., Giavalisco, M., Vanzella, E., et al. 2020, *ApJ*, **888**, 109  
 Jones, L. H., Barger, A. J., & Cowie, L. L. 2021, *ApJ*, **908**, 222  
 Jones, L. H., Barger, A. J., Cowie, L. L., et al. 2018, *ApJ*, **862**, 142  
 Jung, I., Ferguson, H. C., Hayes, M. J., et al. 2024, *ApJ*, **971**, 175  
 Koekemoer, A. M., Faber, S. M., Ferguson, H. C., et al. 2011, *ApJS*, **197**, 36  
 Kokorev, V., Brammer, G., Fujimoto, S., et al. 2022, *ApJS*, **263**, 38  
 Kriek, M. T., Shapley, A. E., Reddy, N. A., et al. 2015, *ApJS*, **218**, 15  
 Kron, R. G. 1980, *ApJS*, **43**, 305  
 Kulkarni, G., Keating, L. C., Haehnelt, M. G., et al. 2019, *MNRAS*, **485**, L24  
 Kurk, J., Cimatti, A., Daddi, E., et al. 2013, *A&A*, **549**, A63  
 Le Fèvre, O., Tasca, L. A. M., Cassata, P., et al. 2015, *A&A*, **576**, A79  
 Le Fèvre, O., Vettolani, G., Garilli, B., et al. 2005, *A&A*, **439**, 845  
 Leitherer, C., Ferguson, H. C., Heckman, T. M., & Lowenthal, J. D. 1995, *ApJL*, **454**, L19  
 Lilly, S. J., Fvre, O. L., Renzini, A., et al. 2007, *ApJS*, **172**, 70  
 Mackenty, J. W., & Smith, L. 2012, CTE White Paper, June 29 Tech. Rep., STScI  
 Malkan, M. A., Webb, W., & Konopacky, Q. 2003, *ApJ*, **598**, 878  
 Marchi, F., Pentericci, L., Guaita, L., et al. 2017, *A&A*, **601**, A73  
 Marchi, F., Pentericci, L., Guaita, L., et al. 2018, *A&A*, **614**, A11  
 Mascia, S., Pentericci, L., Calabro, A., et al. 2023, *A&A*, **672**, A155  
 Masters, D. C., Stern, D. K., Cohen, J. G., et al. 2019, *ApJ*, **877**, 81  
 Momcheva, I. G., Brammer, G. B., Dokkum, P. G. v., et al. 2016, *ApJS*, **225**, 27  
 Mostardi, R. E., Shapley, A. E., Nestor, D. B., et al. 2013, *ApJ*, **779**, 65  
 Naidu, R. P., Forrest, B., Oesch, P. A., Tran, K.-V. H., & Holden, B. P. 2018, *MNRAS*, **478**, 791  
 Naidu, R. P., Matthee, J., Oesch, P. A., et al. 2021, *MNRAS*, **510**, 4582  
 Naidu, R. P., Oesch, P. A., Reddy, N. A., et al. 2017, *ApJ*, **847**, 12  
 Naidu, R. P., Tacchella, S., Mason, C. A., et al. 2020, *ApJ*, **892**, 109  
 Nandra, K., Laird, E. S., Aird, J. A., et al. 2015, *ApJS*, **220**, 10  
 Nayyeri, H., Hemmati, S., Mobasher, B., et al. 2017, *ApJS*, **228**, 7  
 Nestor, D. B., Shapley, A. E., Kornei, K. A., Steidel, C. C., & Siana, B. D. 2013, *ApJ*, **765**, 47  
 Nestor, D. B., Shapley, A. E., Steidel, C. C., & Siana, B. D. 2011, *ApJ*, **736**, 18  
 Newman, J. A., Cooper, M. C., Davis, M., et al. 2013, *ApJS*, **208**, 5  
 Oesch, P. A., Montes, M., Reddy, N., et al. 2018, *ApJS*, **237**, 12  
 Oke, J. B., & Gunn, J. E. 1983, *AJ*, **266**, 713  
 Pahl, A. J., Shapley, A. E., Steidel, C. C., Chen, Y., & Reddy, N. A. 2021, *MNRAS*, **505**, 2447  
 Pentericci, L., Garilli, R. J. M. B., Cucchiati, O., et al. 2018, *A&A*, **616**, A174  
 Popesso, P., Dickinson, M., Nonino, M., et al. 2009, *A&A*, **494**, 443  
 Prichard, L. J., Rafelski, M., Cooke, J., et al. 2022, *ApJ*, **924**, 14

- Rafelski, M. A., Teplitz, H. I., Gardner, J. P., et al. 2015, *AJ*, **150**, 31
- Reddy, N. A., Steidel, C. C., Erb, D. K., Shapley, A. E., & Pettini, M. 2006, *ApJ*, **653**, 1004
- Redshaw, C., McCabe, T., Otteson, L., et al. 2022, *RNAAS*, **6**, 63
- Rivera-Thorsen, T. E., Dahle, H., Chisholm, J., et al. 2019, arXiv:1904.08186
- Robertson, B. E., Ellis, R. S., Furlanetto, S. R., & Dunlop, J. S. 2015, *ApJL*, **802**, L19
- Robertson, B. E., Furlanetto, S. R., Schneider, E. E., et al. 2013, *ApJ*, **768**, 71
- Rutkowski, M. J., Scarlata, C., Henry, A. L., et al. 2017, *ApJ*, **841**, L27
- Saxena, A., Pentericci, L., Ellis, R. S., et al. 2022, *MNRAS*, **511**, 120
- Science Software Branch at STScI 2012, PyRAF: Python alternative for IRAF, Astrophysics Source Code Library, ascl:1207.011
- Shapley, A. E., Steidel, C. C., Strom, A. L., et al. 2016, *ApJL*, **826**, L24
- Siana, B., Shapley, A. E., Kulas, K. R., et al. 2015, *ApJ*, **804**, 17
- Siana, B. D., Teplitz, H. I., Colbert, J. W., et al. 2007, *ApJ*, **668**, 62
- Siana, B. D., Teplitz, H. I., Ferguson, H. C., et al. 2010, *ApJ*, **723**, 241
- Skelton, R. E., Whitaker, K. E., Momcheva, I. G., et al. 2014, *ApJS*, **214**, 24
- Smith, B. M., Windhorst, R. A., Jansen, R. A., et al. 2018, *ApJ*, **853**, 191
- Smith, B. M., Windhorst, R. A., Cohen, S. H., et al. 2020, *ApJ*, **897**, 41
- Smith, B. M., Windhorst, R. A., Teplitz, H., et al. 2024, Lyman Continuum Emission from AGN at  $2.3 \lesssim z \lesssim 3.7$  in the UVCANDELS Fields, arXiv:2401.03094
- Stark, D. P. 2016, *ARA&A*, **54**, 761
- Stefanon, M., Labb, I., Bouwens, R. J., et al. 2017a, arXiv:1706.04613
- Stefanon, M., Yan, H.-J., Mobasher, B., et al. 2017b, *ApJS*, **229**, 32
- Steidel, C. C., Bogosavljevic, M., Shapley, A. E., et al. 2018, *ApJ*, **869**, 123
- Steidel, C. C., Pettini, M., & Adelberger, K. L. 2001, *ApJ*, **546**, 665
- Sun, L., Wang, X., Teplitz, H. I., et al. 2024, *ApJ*, **972**, 8
- Szalay, A. S., Connolly, A. J., & Szokoly, G. P. 1999, *AJ*, **117**, 68
- Szokoly, G. P., Bergeron, J., Hasinger, G., et al. 2004, *ApJS*, **155**, 271
- Teplitz, H. I., Rafelski, M. A., Kurczynski, P., et al. 2013, *AJ*, **146**, 159
- Trump, J. R., Impey, C. D., Elvis, M., et al. 2009, *ApJ*, **696**, 1195
- Vanzella, E., Balestra, I., Gronke, M., et al. 2016, **465**, 3803, arXiv:1607.03112
- Vanzella, E., Calura, F., Meneghetti, M., et al. 2018, arXiv:1809.02617
- Vanzella, E., Castellano, M., Bergamini, P., et al. 2022, *A&A*, **659**, A2
- Vanzella, E., Cristiani, S., Dickinson, M. E., et al. 2007, *A&A*, **478**, 83
- Vanzella, E., Giavalisco, M., Inoue, A. K., et al. 2010, *ApJ*, **725**, 1011
- Vanzella, E., Guo, Y., Giavalisco, M., et al. 2012, *ApJ*, **751**, 70
- Vasei, K., Siana, B. D., Shapley, A. E., et al. 2016, *ApJ*, **831**, 38
- Wang, X., Teplitz, H., Alavi, A., et al. 2020, AAS Meeting Abstracts, **235**, 426.03
- Wang, X., Jones, T., Vulcani, B., et al. 2022a, *ApJL*, **938**, L16
- Wang, X., Li, Z., Cai, Z., et al. 2022b, *ApJ*, **926**, 70
- Windhorst, R. A., Cohen, S. H., Hathi, N. P., et al. 2011, *ApJS*, **193**, 27
- Wirth, G. D., Willmer, C. N. A., Amico, P., et al. 2004, *AJ*, **127**, 3121
- Wirth, G. D., Trump, J. R., Barro, G., et al. 2015, *AJ*, **150**, 153
- Xue, Y., Luo, B., Brandt, W. N., et al. 2016, *ApJS*, **224**, 15
- Yuan, F.-T., Zheng, Z.-Y., Lin, R., Zhu, S., & Rahna, P. T. 2021, *ApJ*, **923**, L28